

THE SEYFERT-STARBURST CONNECTION IN X-RAYS. I. THE DATA

N. A. LEVENSON, K. A. WEAVER¹, AND T. M. HECKMAN

Department of Physics and Astronomy, Bloomberg Center, Johns Hopkins University, Baltimore, MD 21218

To appear in the Astrophysical Journal Supplement Series, April 2001

ABSTRACT

We analyze X-ray spectra and images of a sample of Seyfert 2 galaxies that unambiguously contain starbursts, based on their optical and UV characteristics. Although all sample members contain active galactic nuclei (AGNs), supermassive black holes or other related processes at the galactic centers alone cannot account for the total X-ray emission in all instances. Eleven of the twelve observed galaxies are significantly resolved with the *ROSAT* HRI, while six of the eight sources observed with the lower-resolution PSPC also appear extended on larger scales. The X-ray emission is extended on physical scales of 10 kpc and greater, which we attribute to starburst-driven outflows and supernova-heating of the interstellar medium. Spectrally, a physically-motivated composite model of the X-ray emission that includes a heavily absorbed ($N_H > 10^{23} \text{ cm}^{-2}$) nuclear component (the AGN), power-law like scattered AGN flux, and a thermal starburst describes this sample well. Half the sample exhibit iron $K\alpha$ lines, which are typical of AGNs.

Subject headings: galaxies: Seyfert — X-rays: galaxies

1. INTRODUCTION

One of the most important questions about Seyfert galaxies is the fundamental nature of their energy source. While accretion onto supermassive black holes generally describes successfully the central engines of many Seyfert galaxies (e.g., Miyoshi et al. 1995, Tanaka et al. 1995, and Nandra et al. 1997), starbursts are also important, often in the same galaxies. The bolometric luminosity of circumnuclear starbursts can be comparable to active galactic nuclei (AGNs; Genzel et al. 1998). Other observations suggest that the AGN and starburst phenomena may be directly related on cosmological scales. At low redshift ($z < 2$), the populations of quasars and star-forming galaxies evolve similarly (Boyle & Terlevich 1998 and references therein), and masses of black holes in galactic centers are strongly correlated with the velocity dispersions of their “host” stellar spheroids (Gebhardt et al. 2000; Ferrarese & Merritt 2000).

Accretion alone does not fully account for the variety of emission observed in AGNs. In particular, much of the optical and ultraviolet emission from type 2 Seyfert galaxies is a featureless continuum that *cannot* be light from an obscured Seyfert 1 nucleus that is scattered off dust or warm gas, as optical spectropolarimetry (Tran 1995a,b,c) and UV spectroscopy (Heckman et al. 1995) demonstrate. Two possibilities have been advanced for the origin of the featureless continuum: optically-thin thermal emission from warm gas in the reflection region (Tran 1995a,b,c) or light from a circumnuclear starburst (Cid Fernandes & Terlevich 1995; Heckman et al. 1995). UV images and high-quality optical and UV spectra of a flux-limited sample of type 2 Seyfert nuclei (Heckman et al. 1995, 1997; González Delgado et al. 1998; González Delgado, Heckman, & Leitherer 2000) strongly suggest that there are two types of Seyfert 2s. In roughly half the sample nuclei, a strong UV continuum shows the unambiguous spectroscopic signature of hot stars. These are the Seyfert/starburst (Sy2/SB)

composite galaxies. In the other members of the sample, the UV continuum is relatively faint and sometimes has a cone-like structure aligned with the radio axis. In these latter, the nuclear UV light is probably due to a combination of scattered light and optically-thin thermal emission from warm (10^5 to 10^6 K) gas in the reflection region.

X-ray spectroscopy is a valuable tool for investigating the Seyfert-starburst connection. The soft X-ray emission in about one-third of Seyfert 2 galaxies is thermal (Turner et al. 1997), and this emission is consistent with the soft X-ray properties of nearby starbursts (Dahlem, Weaver, & Heckman 1998; Weaver et al. 2000). At energies of 1–2 keV, emission from X-ray binaries and individual supernova remnants dominates in starbursts, while at lower energies, thermal emission from diffuse gas that has been heated to temperatures of 0.2 to 1.0 keV by the collective effect of stellar winds and supernovae (e.g., McKee & Ostriker 1977) is the primary source of X-ray emission. This hot gas can escape the starburst in the form of a galactic “superwind” (Chevalier & Clegg 1985; Heckman, Lehnert, & Armus 1993).

Because hard X-rays can penetrate large column densities of gas and dust, they serve as direct observational probes of deeply buried Seyfert 1 nuclei in Seyfert 2 galaxies, which the unified model suggests. (See Antonucci 1993 and Urry & Padovani 1995 for reviews.) In the unified model, the X-ray emission in a type 2 Seyfert nucleus consists of the sum of the heavily-absorbed power-law emission from the hidden Seyfert 1 that has been transmitted through the torus and the lightly-absorbed power-law emission that has been reflected off the mirror. In the composite objects, both the buried Sy 1 and the starburst produce X-rays. While the AGN dominates the Sy2/SB spectra at high energies, below around 2 keV the reflected and transmitted X-ray emission of the AGN are combined with the soft thermal spectrum of the starburst compo-

¹ Laboratory for High Energy Astrophysics, Code 662, NASA/GSFC, Greenbelt, MD 20771

ment.

This is the first of two papers in which we investigate the X-ray signatures of the Seyfert-starburst connection. In this work, we discuss our analysis of the X-ray images and spectra of a sample of known Sy2/SB composites. We present X-ray images and spectra obtained with both *ROSAT* and *ASCA* of this sample in §2. We do not expect the unresolved active nucleus to be the sole source of X-ray emission in each galaxy and examine the images for extended emission (§3). We fit the spectra with complex models that are physically motivated (§4). We comment on individual galaxies in §5 and draw conclusions in §6. In Levenson, Weaver, & Heckman (2000; Paper II), we compare the X-ray properties of these composites to “pure” starbursts and Seyferts and discuss the implications for the connection between AGNs and starbursts.

2. THE DATA

2.1. Selection Criteria

For our study, we have chosen galaxies from the Heckman et al. (1995) sample. In order to investigate how the starburst phenomenon relates to Seyfert 2s, these authors identified the 30 brightest Seyfert 2 nuclei based on [O III] $\lambda\lambda 4959 + 5007$ emission line flux and nuclear nonthermal monochromatic flux (νF_ν) at 1.4 GHz from the compilation of Whittle (1992). Members of the Heckman et al. (1995) sample have either $\log F_{[\text{OIII}]} \geq -12.0 \text{ erg cm}^{-2} \text{ s}^{-1}$, or $\log F_{1.4} \geq -15.0 \text{ erg cm}^{-2} \text{ s}^{-1}$, or both.

A starburst is evident in approximately half of these bright Seyfert 2 galaxies. They have the spectroscopic signatures of luminous young stars, such as stellar wind lines, Balmer absorption, and broad Wolf-Rayet emission features (Heckman et al. 1997; Wang, Heckman, & Lehnert 1997; Cid Fernandes, Storchi-Bergmann, & Schmitt 1998; González Delgado et al. 1998; Schmitt, Storchi-Bergmann, & Cid Fernandes 1999; González Delgado et al. 2000). We restrict our sample to these known Seyfert/starburst composites plus several galaxies that Heckman et al. (1995) had excluded from their study only because IUE had not observed them but which fulfill the original selection criteria. Our sample is unbiased, but we exclude several known composite galaxies that were not part of the original Whittle (1992) sample or that fail to meet the brightness criterion.

The optical properties of the sample are listed in Table 1. The objects are listed in order of right ascension (J2000). Distances (column 4) are calculated assuming $H_0 = 75 \text{ km s}^{-1} \text{ Mpc}^{-1}$. The scale (in pc) is equivalent to 1'' (column 5). The galaxy inclinations (column 7) should be interpreted cautiously. They have been determined assuming circular disk geometry, yet many of these are disturbed systems, for which this method is inappropriate. The references for Galactic column density, inclination, and starburst activity for each galaxy are noted. Table 2 contains information on the X-ray observations we present here, which we describe in detail subsequently.

2.2. ROSAT HRI Observations

The *ROSAT* High Resolution Imager (HRI) is a particularly appropriate tool for identifying extended nuclear emission. In addition to the advantage of its absolute spatial resolution, its sensitivity is greatest at the soft energies

typical of the widespread thermal emission of starburst galaxies. We have obtained HRI data for all 14 members of the sample, although two of the exposure times were too short to provide any useful information (Mrk 463 and NGC 7674). We use an off-source region in each field to determine the constant background to subtract. The background-subtracted HRI count rates are listed in column 4 of Table 2.

Figure 1 illustrates the relationship of the soft X-ray and optical emission in these objects and the radial distribution of the soft X-rays. The HRI images are constructed from the raw (0''.5) pixels, smoothed with a two-dimensional Gaussian of FWHM = 4''. The alignment is based on the *ROSAT* pointing and astrometry of the Digitized Sky Survey (DSS) frames. When additional point sources are located within the complete observed field, they are used to improve the alignment. Because members of the sample themselves may be extended X-ray sources, we do not use them to correct the astrometry. The optical and X-ray alignment of Mrk 1073 is uncertain. Based on the *ROSAT* telescope pointing alone, the X-ray source appears offset 25'' from the optical location of Mrk 1073. No other sources are detected in the field, so we have approximated the alignment of the images.

We extracted images at the full spatial resolution of the HRI in order to identify extended emission, comparing the observed radial profile with the theoretical point spread function (PSF; David et al. 1999). A two-dimensional Gaussian fit to each smoothed image defines the center of emission. We combined the raw 0''.5 pixels into 3'' bins to construct the radial profile, fitting the amplitude and background to the data. In no case is the target galaxy or any other source in the field bright enough to correct for errors in the telescope pointing (cf. Morse 1994). When known point sources appeared in the field, however, we compared their observed radial profiles to check the consistency of our results.

2.3. ROSAT PSPC Observations

ROSAT PSPC observations provide spatial and spectral information on some of these Sy2/SB composites. All the sources were the specified central targets of the observations, so they are located at the centers of the observed PSPC fields and do not require vignetting corrections. We subtracted a constant background, measured over a large central region excluding the source, to determine the count rates listed in column 7 of Table 2.

PSPC contours overlaid on optical images are shown for Mrk 463 and NGC 7674, the sources for which we lack adequate HRI data (Figures 2 and 3). Figure 4 contains the PSPC radial profiles. We use the same technique described for the HRI data above to identify extended soft X-ray emission in the PSPC observations, applying the appropriate theoretical point spread function, assuming typical energy of 1 keV (Hasinger et al. 1992).

We examined the soft (0.2–0.4 keV) and hard (0.4–2.0 keV) PSPC bands separately, as well as the total emission. We present these broad-band images (Figures 5–8) in the cases in which we measure significant differences.

Spectra were extracted from circular regions of 2' radius typically, except in crowded fields. Some sample members

contain double nuclei, which are separated by a few arcseconds or less and are therefore unresolved. Thus, the contributions of both nuclei are combined in the resulting spectra. Nearby, source-free regions of the sky were used to determine the background. The data are grouped so that each bin has a minimum of 30 counts, and therefore χ^2 statistics are appropriate in the model fits. Spectral models were fit from 0.2 to 2.0 keV using the appropriate response matrices. The low-energy sensitivity of the PSPC is particularly useful to detect the soft thermal emission of the starburst and to constrain the absorbing column density along the line of sight.

2.4. *ASCA* Observations

We use the *ASCA* observations of these composite galaxies to identify their AGN and starburst components spectrally. See Tanaka, Inoue, & Holt (1994) for a description of the *ASCA* experiment. We processed the *ASCA* data to exclude times of high background rates. The accepted data were taken outside of and greater than 16 s after passages through the South Atlantic Anomaly, at elevations above the Earth's limb greater than 5° , at times greater than 16 s after a satellite day/night transition, and with geomagnetic cutoff rigidity greater than 6 Gev c^{-1} . Source counts were extracted from circular regions having a radius approximately 3/2 on the SIS detectors (SIS0 and SIS1) and 4/4 on the GIS detectors (GIS2 and GIS3), appropriate to the instrumental resolution. Source-free regions of each detector were used for the corresponding background measurements. The *ASCA* count rates and SIS mode are listed in columns 10 and 11 of Table 2. The *ASCA* spectra were binned according to the same criterion as the PSPC spectra. We include SIS data for energies in the range 0.6 to 10.0 keV, and GIS data in the range 0.7 to 10.0 keV. We model the spectra with the latest *ASCA* effective area calibration. All models include a constant factor to account for the few percent known difference in the SIS and GIS fluxes. The fluxes and normalizations listed in the tables are for the SIS0 detector.

Several of the galaxies are variable (NGC 5135, Mrk 463, NGC 6221, and NGC 7582), typically showing flux changing by factors of less than 50% on timescales on the order of 10^4 s. Our concern here, however, is using high signal-to-noise data to determine the net properties of these galaxies, so we use the time-averaged spectra for each pointing. Furthermore, most of the variability is evident at high energies and does not affect the soft starburst emission that we emphasize. Mrk 477 was observed on two separate occasions. We found no variation between these observations, so we have combined the two data sets. NGC 7582 was also observed twice. The spectrum varied significantly around energies $2 \lesssim E \lesssim 3 \text{ keV}$ (Xue et al. 1998), so we have treated the two data sets independently. The soft X-ray emission in the *ASCA* bandpass does not vary, so we have used the same PSPC spectrum in the joint fits of data from both satellites.

3. IMAGING RESULTS

3.1. *ROSAT* Images

We summarize the results of detecting extended X-ray emission in the *ROSAT* data in Table 3. We use the maximum radius at which residual flux is detected to approx-

imate the physical scale of the extended emission in HRI and PSPC observations (columns 2 and 5, respectively). Subtracting the best-fitting theoretical PSF from the observed values, we estimate the fraction of total flux that is in excess of a single, central point source using two techniques. The radial profile plots (Figures 1 and 4) and columns 3 and 6 of Table 3 contain the results of the first method, in which we fit the entire PSF weighted by the Poisson errors. These residuals tend to be extremely small or negative at the smallest radii and increase at larger radii. The residual profile corresponds to the intrinsic shape of the non-AGN flux, which here implies rings of emission in the two-dimensional images. Such unfilled rings are unlikely to generally represent the true physical structure of the extended components. Thus, this method overestimates the unresolved emission and yields conservative estimates of the minimum extended fraction in each galaxy. The associated errors printed in the table are derived from Monte Carlo simulations of this technique and do not reflect its systematic bias in favor of the AGN contribution. In the second method (columns 4 and 7 of Table 3), we require that the residual distribution be flat within the central core of the PSF. This constraint is more realistic when truly extended emission is present and also fits unresolved sources well. A disadvantage is that the errors associated with this technique are somewhat larger than those of the first method. As a result, the HRI observation of NGC 7130, for example, is resolved according to the first estimate, but we determine only an upper limit on the extended fraction using the more realistic model.

The X-ray emission from three galaxies (Mrk 1066, Mrk 273, and Mrk 477) is unresolved in the HRI data, according to the conservative estimates. Using the constrained model, Mrk 273 and Mrk 477 are resolved. Only in the case of Mrk 1066 do we fail to find any evidence for extended emission. In all other galaxies observed with the HRI, the soft X-ray emission cannot be attributed to a single point source alone. At the lower spatial resolution of the PSPC, six galaxies are extended: NGC 1068, Mrk 78, NGC 5135, Mrk 266, NGC 7582, and NGC 7674. The counting statistics as well as the intrinsic resolution are particular limitations in the observations of Mrk 78 and NGC 7674. Mrk 78 is significantly resolved only according to the constrained (second) method. In the case of NGC 7674, only using the first method are the errors small enough to determine that the emission is extended with confidence.

The HRI and PSPC are sensitive to extended emission on different angular scales. The resolution of the PSPC is around $30''$, so it is suited for measuring large angular scales. The resolution of the HRI is around $5''$, but it is not as sensitive as the PSPC. It cannot detect the extremely low surface brightness of the most extended emission, such as that due to a starburst-driven superwind, but it does resolve brighter, more distant sources. While our results suggest that the PSPC is optimized for detecting extended emission at radii of $50''$, the HRI generally only detects extended emission out to radii of $20\text{--}30''$. Therefore, the combination of resolution, sensitivity and varying galaxy distances biases the physical scales on which we can actually measure extended emission with the PSPC and HRI.

The galaxies that are significantly resolved in the total PSPC images also exhibit distinct morphology in the soft

and hard energy regimes. The softest emission from NGC 1068 is not very centrally concentrated (Figure 5a). The emission profile is flat, not sharply peaked. At harder energies, NGC 1068 is strongly centrally concentrated, and the low surface brightness emission extends toward the northeast and southwest (Figure 5b). Although the PSF of the PSPC has a broader core at lower energies, this energy dependence alone does not account for the observed difference. We detect truly distinct morphologies in the soft and hard emission. The hard emission from NGC 5135 is symmetric and centrally concentrated, while in this galaxy the soft emission is more diffuse and irregular (Figure 6). The low-energy image of Mrk 266 consists of two distinct sources (Figure 7a). The galaxy’s nuclei account for the southern component, while the additional extended emission also detected in the HRI observation coincides with the northern source. Only the southern component is significant at higher PSPC energies (Figure 7b). The southern component is resolved in both energy bands, supporting its identification as the compound nucleus. The soft emission of NGC 7582 (Figure 8a) is extremely diffuse and extends mostly perpendicular to the plane of the galaxy, as expected from a superwind. In this case, the hard emission is sharply peaked at the nucleus and extends primarily in the galactic disk (Figure 8b).

3.2. *ASCA* Images

We constructed images from the *ASCA* data in two noteworthy cases: Mrk 273 and NGC 7582. Both have X-ray “companions” that appear nearby projected onto the plane of the sky but are not physically associated with the galaxies of interest. Mrk 273 and its companion, Mrk 273X, separated by about $2'$, are clearly resolved by the HRI and PSPC (Figure 9). The latter contributed about one-third of the soft X-ray flux in the PSPC observation of 1992 May (Turner et al. 1993) and HRI observation in 1992 June, but faded significantly by 1994 December, when *ASCA* observed the field. We can distinguish Mrk 273 and Mrk 273X in the SIS data because the point spread function has a sharp central core. The companion contributes less than 10% of the total SIS0 counts, mostly in the soft (0.5–2 keV) band. NGC 7582 and its companion are also separated by about $2'$ and resolved in HRI (Schachter et al. 1998) and PSPC images (Figure 10). This companion is much fainter than NGC 7582, contributing only 15% of the total counts. It is relatively stronger at soft energies, having 30% of the flux of NGC 7582 in the SIS0 detector. Note that in both of these cases, the companions do not significantly affect the results of spectral modelling.

4. SPECTRAL MODELLING

While fitting spectral models to the data, we are ultimately guided by the realistic physical conditions in the sample galaxies. While the AGNs emit characteristically strong X-rays, we know that these are not the only X-ray sources present. The images clearly reveal extended soft X-ray emission, which cannot be due to the active nuclei. Because all the sample members definitely contain starbursts, we expect thermal X-ray emission from these, by analogy with ordinary starburst galaxies that lack AGN.

We develop the complex models that account for the multiple physical sources gradually, however, beginning

with several simple models that we apply to all the spectra. Although not all models are realistic for every galaxy, by systematically building complex models out of the likely components, we demonstrate which pieces are significant in different cases. Also, the uniform set of models facilitates comparison of the sources, even in the instances where we obviously require multi-component models to achieve good fits, such as NGC 1068. We present model fits to *ASCA* data first and then joint fits with the PSPC data, when available. For Mrk 78 and NGC 7674, which lack *ASCA* data, only PSPC fits are presented.

4.1. *Power-law Models*

We first examine a single absorbed power law, where the photon index and absorbing column density are left as free parameters, although the absorption is constrained to be greater than or equal to the Galactic value. This sort of model tends to approximate well the spectra of Seyfert 1 galaxies. For most of the composite objects, however, this model (Model 1) either fits the data poorly or produces unphysical results (Table 4). The derived photon indices tend to be small and the model generally fails to account for the observed soft X-ray emission. None of the single power law fits to *ASCA* spectra are acceptable.

To better model the soft emission, we try various solutions that are physically motivated. First, we examine adding a second power law component (Model 2), which represents the case of a buried Seyfert nucleus with material that scatters a significant amount of the blocked soft X-ray emission in our direction:

$$I(\text{photons s}^{-1} \text{cm}^{-2} \text{keV}^{-1}) = \exp(-N_{H0}\sigma_{abs}) (\exp(-N_{H1}\sigma_{abs})(A_1 E^{-\Gamma}) + A_2 E^{-\Gamma}), \quad (1)$$

where N_{H0} and N_{H1} are the Galactic and nuclear column densities, respectively, σ_{abs} is the absorption cross-section, A_1 and A_2 are the magnitudes of the intrinsic and scattered components, respectively, and Γ is the photon index. In this case, the soft X-ray photon index is set equal to the hard X-ray (nuclear) index, the column density toward the scattered component is fixed at the Galactic value, and the nuclear column density is a free parameter. In addition, we fix the photon indices at 1.9, the mean value for the *intrinsic* index for Seyfert 1 galaxies (Nandra & Pounds 1994). With the exception of NGC 1068 and NGC 6221, all objects prefer this model over the single power law, with a distinct, heavily absorbed component having $N_H > 10^{23} \text{cm}^{-2}$ (where $N_H = N_{H0} + N_{H1}$) indicated in all cases, either by direct observation or inferred by the presence of strong Fe $K\alpha$ fluorescence, which is produced in a region of high column density. In addition, the extra soft X-ray power law component accounts for most of the residual error. Several fits are very good; for example, $\chi^2/\text{dof} \approx 1.1$ for Mrk 1066, Mrk 273, and Mrk 463 (Table 5).

4.2. *Thermal Plasma Models*

Next we examine a model that replaces one of the power law components with a thermal plasma having solar abundances (Model 3). Physically, this represents the soft X-ray emission due to starburst activity. In addition to the possible transmitted and reflected AGN components, some source of emission that can be extended is required

for consistency with the soft X-ray emission resolved with *ROSAT*. For the thermal component we use the so-called “MEKAL” model of Mewe and Kaastra (Mewe, Gronenschild, & van den Oord 1985; Arnaud & Rothenflug 1985; Mewe, Lemen, & van den Oord 1986; Kaastra 1992), with updated Fe L calculations (Liedahl 1992). Our intention is to determine whether a thermal model better describes the soft X-ray emission than a power law model. Model 3 yields a better fit than Model 2 for 6 of 13 ASCA observations and for 4 of 7 cases where PSPC data are available, for a total of 7 galaxies (Table 6). For cases where the fits are worse, they can be improved by reducing the metal abundance, but since abundances are difficult to estimate from data of this quality, we do not pursue this option.

Finally, we examine three-component models that combine Model 2 with thermal emission. In addition to the original power law, this model (Model 4) contains a second power law, to represent scattered flux, and a thermal component to model the soft X-ray emission, which might be expected from a combination of an AGN and starburst. Table 7 lists these results only for the cases where this model significantly improves the fit. The three-component model improves the fits over Models 1 or 2 significantly in 5 out of 13 cases for *ASCA* fits and in 6 out of 7 cases for joint fits, for a total of 6 out of 12 galaxies with *ASCA* data.

4.3. Best-Fitting Models

Table 8 contains a summary of the best-fitting model for each galaxy, including a Gaussian to model the Fe K α line (discussed below) in cases where it is detected. For non-detections, upper limits on the line equivalent widths (EWs) are noted. In each case, the inclusion of additional components or variable parameters over models with fewer free parameters is statistically significant at the 90% confidence level, based on an F test. The data and model fits are displayed in Figure 11. Although we used both SIS and both GIS detectors independently in the model fitting, we plot the average of data from the SIS detectors and the average of data from the GIS detectors separately for clarity. Both *ROSAT* and *ASCA* spectra are shown where they are available.

Although the spectra of Mrk 1073 and IC 3639 are of low statistical quality, we can use their images to infer which process dominates the soft X-ray spectrum. Throughout the sample, the objects with the strongest thermal spectra, such as NGC 5135, tend to be most extended. The soft X-rays are resolved in Mrk 1073 and IC 3639, so the most likely spectral model for both is thermal emission. Specifically, because Mrk 1073 is not a point source, we have adopted Model 3 as the best fit, but Model 2 also formally fits well and explicitly illustrates the heavily obscured ($N_H \sim 10^{24} \text{ cm}^{-2}$) AGN. In the case of IC 3639, although statistical improvement of the complex model (Model 4) over the preferred Model 3 is not significant, we learn from it that the scattered contribution in this galaxy is relatively weak. Hence, the single power law we observe in this best-fitting model is the intrinsic nucleus.

We experimented with several modifications to the basic models. For example, NGC 1068 has an extremely complex spectrum (Ueno et al. 1994; Iwasawa, Fabian, & Matt 1997), and we require several emission lines and multiple

thermal components to fit it adequately. The PSPC is very sensitive to small changes in N_H , and increasing the low-energy column density improves some of the fits. This is the case for NGC 7582, so we have allowed the soft N_H to be free for all fits to this galaxy. Mrk 273 also prefers absorption that is slightly higher than the Galactic value, but since this does not affect our results in a significant manner, we use only the Galactic value for N_H in the fits presented here.

We have only PSPC spectra of Mrk 78 and NGC 7674. We considered several models of their soft emission, including a power law, thermal emission, and combinations of the two. In each case, a single component with Galactic absorption best fits the data. This component is a thermal plasma in Mrk 78 and a power law in NGC 7674. The parameters of these models are listed in Table 9.

4.4. Fe K α Emission

Fe K α emission is common to active galaxies. In many cases, particularly Seyfert 1s, the lines are broadened by Doppler and relativistic effects, indicating that a significant component of the line originates in the inner regions of an accretion disk (Nandra et al. 1997). Seyfert 2 galaxies, on the other hand, often show narrow features, which appear to originate farther out in the galaxy, perhaps due to fluorescence of the nuclear continuum in the obscuring torus (Weaver et al. 1996). In any case, the profile and variability of the iron line can tell us a great deal about the physics of the gas that is fueling the AGN.

Several members of our Seyfert/starburst sample exhibit Fe K α lines. Since the iron lines are not the focus of this paper, we consider modeling the lines only in the best-fitting of the previous models (Table 8). Typically, the Fe K lines are narrow and can be fitted with an unresolved Gaussian with $\sigma < 0.05$ keV. We measure equivalent widths with respect to the power law component responsible for the hard X-ray emission. For cases where this component physically represents the intrinsic (yet absorbed) power law, the EW ranges from approximately 100 eV to 1 keV. In several cases (e.g., NGC 1068, Mrk 1066), however, this intrinsic AGN is not detected directly because it is completely absorbed. In these galaxies, the only detectable hard X-ray continuum is due to the scattered power law. As a result, measuring these EWs with respect to the genuinely weaker scattered (rather than intrinsic) AGN, we find these EWs to be large, greater than 3 keV. In these cases, we crudely estimate the line EW with respect to the intrinsic AGN continuum, assuming the mean fraction of intrinsic emission that is measured to be scattered in the other sample members indicates the true intrinsic component. This average scattering fraction $f_{scatt} = 0.05$. Thus, increasing the continuum by a factor of 20, we predict the EW with respect to the intrinsic continuum to be 50 and 160 eV in NGC 1068 and Mrk 1066, respectively. The corresponding upper limits are EW $< 50, 470, \text{ and } 270$ eV in IC 3639, Mrk 266, and NGC 7130, respectively.

NGC 6221 is unusual in that it contains a broad line with $\text{EW} \approx 400$ eV. We find $\sigma = 0.5(+0.4, -0.02)$ keV with 90% confidence. The Fe line properties of this galaxy are more characteristic of Seyfert 1s, where the reprocessing material is close to the galaxy nucleus. The absorption of the

hard component in NGC 6221 is only 10^{22} cm^{-2} , which is much lower than in any other members of the sample. As a result, although this galaxy possesses both the scattered power law and thermal soft X-ray emission typical of other Sy2/SB composites, the intrinsic AGN dominates the observed X-ray emission at low and high energies during the *ASCA* observation.

The strength of the Fe K line is related to the column density of the fluorescing material in a predictable fashion. The uncertainty in studying this relation has historically been due a lack of reliable measurements of N_H , especially for very large column densities ($N_H \gtrsim 10^{23} \text{ cm}^{-2}$). In Figure 12, we plot Fe K EW versus N_H for our sample (solid symbols). By measuring the line with respect to the intrinsic continuum, where we account for both the absorbed X-ray emission from the AGN and the scattered flux, we find that the EWs are similar to those expected for the inferred column densities. For comparison, we also plot the results from Turner et al. (1997; open symbols), which were derived using the observed continuum. Theoretical predictions for spherically-symmetric and torus geometries are plotted with the dashed and dot-dashed lines, respectively. The *ASCA* data are of too poor quality to be able to distinguish between these models, but we conclude that our measurements are consistent with such geometries and that these objects indeed possess buried Seyfert 1 nuclei.

5. NOTES ON INDIVIDUAL GALAXIES

5.1. NGC 1068

NGC 1068 is a member of a group (Garcia 1993) and contains a stellar bar (Thronson et al. 1989). Broad optical emission lines are observed in polarized light (Antonucci & Miller 1985). The X-ray emission from NGC 1068 has been studied in detail (Wilson et al. 1992; Ueno et al. 1994; Iwasawa et al. 1997; Netzer & Turner 1997), and its spectrum is extremely complex.

For consistency, we present the simple model fits to the spectrum, although none of these are satisfactory. The best-fit model includes a power law, two thermal components, and three Gaussian components. The intrinsic power law of the AGN is completely absorbed. In these joint fits of *ASCA* and PSPC data, we have rejected SIS data at energies $E < 0.8 \text{ keV}$, because the SIS calibration of such bright, soft sources at low energies is highly uncertain (Weaver, Gelbord, & Yaqoob 2000). We find that 80% of the soft X-ray emission is thermal.

NGC 1068 is clearly extended in X-ray emission, and the soft and hard PSPC bands are distinct. Although a radio jet has been observed (Wilson & Ulvestad 1982), the extended X-ray emission is associated with the starburst, not the jet (Wilson et al. 1992). Measured both with the HRI and PSPC, the soft X-ray emission extends on scales greater than 7.4 kpc.

5.2. Mrk 1066

Mrk 1066 has a bar but is not a member of a group or cluster.

In the spectrum of Mrk 1066, we observe a single power law component, soft thermal emission, and an Fe line. The thermal emission accounts for half the total soft X-ray flux. The absorption of the power law is consistent with the Galactic column density; this component is due

to the scattered AGN. We do not detect the intrinsic hard AGN emission directly, even at the highest energies of the *ASCA* bandpass. The AGN is heavily absorbed, with $N_H > 10^{24} \text{ cm}^{-2}$. Because the equivalent width of the line is measured with respect to the scattered component, it is large: $EW \approx 3000 \text{ eV}$.

5.3. Mrk 1073

Mrk 1073 is part of the Perseus cluster and paired with UGC 2612. It contains a central bar.

This galaxy lies at the edge of the cluster, complicating background subtraction of the X-ray spectra. We have selected background regions preferentially away from the cluster emission. The signal-to-noise ratio of the SIS1 data is very low, so we have not used these data in the spectral fitting. The best-fitting spectrum consists of a single power law and a thermal contribution. Most (91%) of the soft X-rays are thermal. Although a second power law component instead of thermal emission fits the soft X-ray data equally well, we prefer the thermal model because Mrk 1073 is an extended X-ray source, as observed with the *ROSAT* HRI. The physical scale of this extent is 9.5 kpc.

5.4. Mrk 78

Mrk 78 is a barred galaxy. Its elongated radio and [O III] emission are correlated (Pedlar et al. 1989).

The PSPC spectrum of Mrk 78 is best fit with a thermal plasma, $kT = 0.76 \text{ keV}$, and Galactic absorption. Observed with the HRI, the soft X-ray emission is extended, to a radius of 17 kpc. The PSPC data also suggest extended emission, on a scale of 36 kpc.

5.5. IC 3639

IC 3639 has a bar (Mulchaey et al. 1997) and is paired with ESO 381-G009.

We excluded the low-quality SIS1 data from the spectral fitting. The remaining data are best fit with a two-component model of a power law and thermal emission. The thermal temperature is high, $kT = 2.3 \text{ keV}$. In this case, all the soft X-ray emission is thermal. The three-component model, including the scattered power law, also fits the data. In this case $kT = 1.7 \text{ keV}$, but the improvement to the fit with inclusion of additional parameters is not statistically significant. The X-ray emission is extended in the HRI data, with a radius of 6.8 kpc.

5.6. NGC 5135

NGC 5135 contains a bar, which has also been observed in the near-infrared (Mulchaey et al. 1997), and it is in a group (Kollatschny & Fricke 1989).

NGC 5135 is best fit with the three-component model of a scattered power law and thermal emission. The soft X-ray flux from the thermal component is slightly stronger than that of the scattered power law; 54% of the soft X-ray emission is thermal. The residuals of the fit suggest that an additional low-energy ($E < 0.5 \text{ keV}$) source is present. Analogous to nearby starbursts, this is likely an additional thermal component, but we cannot measure it significantly in the present data. The X-ray emission from

NGC 5135 is extended, both in HRI and PSPC observations, on scales of 5.3 and 13 kpc, respectively, and the soft and hard emission within the PSPC bandpass are spatially distinct.

5.7. Mrk 266

Optically, Mrk 266 contains two nuclei. Both nuclei and more extended emission have been observed in X-rays (Wang et al. 1997; Kollatschny & Kowatsch 1998).

In the spectral modelling, we have excluded SIS1 data. Few counts were obtained in this detector, and the low-energy response is poorly calibrated for the time of the observation in 1999 May. The GIS2 and GIS3 data were combined to increase the signal-to-noise ratio. The best model consists of a power law and thermal emission. The latter accounts for 43% of the soft X-rays. The Galactic column density alone accounts for the absorption of the power law, indicating that we observe only the reflected nucleus and do not detect the buried (under $N_H > 10^{24} \text{ cm}^{-2}$) AGN directly. The upper limit on the Fe K α line equivalent width is correspondingly large (EW < 9400 eV), because it is measured with respect to the reflected rather than intrinsic source.

Mrk 266 is clearly extended in the HRI data, where we detect the two nuclei and further extended emission out to a radius of 22 kpc. This galaxy is also extended at the resolution of the PSPC, in which case $R_{kpc} = 32$, with distinct spatial structure in the hard and soft bands.

5.8. Mrk 273

Mrk 273 is an ultraluminous infrared galaxy and contains two nuclei.

We exclude the poor-quality GIS2 data from the spectral fitting of Mrk 273. The X-ray spectrum is best fit with a four-component model: direct and scattered power law from the AGN, thermal emission from the starburst, and a line. The thermal component provides 43% of the soft X-ray flux. Including the PSPC data, we have also varied the absorbing column of the soft component. We significantly improve the fit by increasing the absorption on the soft components to $3.4(+2.6, -1.2) \times 10^{20} \text{ cm}^{-2}$ from the Galactic value of $9.7 \times 10^{19} \text{ cm}^{-2}$. The temperature of the thermal emission and the relative contributions of the two soft components do not change appreciably in this case.

The HRI data suggest that the X-ray emission from Mrk 273 is extended, not confined to a point source, with $R_{kpc} = 18$.

5.9. Mrk 463

This galaxy has two nuclei, and one of them, Mrk 463E, has been observed to have broad optical lines in polarized light (Miller & Goodrich 1990).

The three-component model of a scattered power law and thermal emission fits Mrk 463. Thermal emission accounts for 31% of the soft X-rays. The theoretical point spread function of the PSPC does not fit Mrk 463 well, suggesting that the X-ray emission is extended on scales of 48 kpc, but the observed radial profile is also consistent with a point source.

5.10. Mrk 477

Mrk 477 has a companion 50'' away, which is connected by tidal tails (Zwicky 1971). Broad optical emission lines are observed in polarized light (Tran et al. 1992).

Mrk 477 is the only member of the sample that has been observed with *ASCA* whose spectrum is not fit best with a model that includes thermal emission. Rather, a scattered power law and narrow line comprise the best-fitting model. When a thermal component is added to this model, the parameters are reasonable— $kT = 0.9 \text{ keV}$ and $A_3 = 9.3 \times 10^{-6}$ —but this addition does not statistically improve the fit. The Galactic column density toward Mrk 477 is low, similar to Mrk 273 and NGC 7582. In those cases, when the column density absorbing the soft X-ray emission is a free parameter, which the PSPC data constrain well, the thermal emission is significant. Observed with the HRI, Mrk 477 is extended to a radius of 15 kpc, measured with the constrained technique (§3.1).

5.11. NGC 6221

NGC 6221 contains a bar, is in a group, and its peculiar morphology may be due to interaction with NGC 6215 (Pence & Blackman 1984). The Sy2 identification of NGC 6221 is based on the [O III]/H β intensity ratio in a blueshifted component of the lines (Veron, Veron, & Zuiderwijk 1981; Pence & Blackman 1984), although using the total optical spectrum of the nucleus, it is classified as a starburst (Cid Fernandes et al. 1998).

We detect both NGC 6221 and ESO 138-1 in the *ROSAT* HRI and *ASCA* GIS images, so the X-ray identification of NGC 6221 is secure, in contrast to the suggestion of Schmitt & Storchi-Bergmann (1995) that these galaxies are confused for one another.

Of the Sy2/SB composites we examine here, NGC 6221 appears most like a Sy1 in X-rays. The absorption is low, $N_H = 1 \times 10^{22} \text{ cm}^{-2}$, so the observed soft X-ray emission includes a dominant (80%) contribution from the intrinsic AGN, as well as the scattered and thermal components. Only 5% of the soft X-ray flux is thermal. The observed Fe line is broad, with EW = 400 eV, centered at 6.6 keV. The EW is relatively large compared with Sy 1 emission lines, and the energy is high, which together suggest an ionized region.

The HRI observation demonstrates that the soft X-ray emission is extended to a radius of 4.8 kpc. This extended emission accounts for half the observed counts, in contrast to the small fraction of thermal soft X-ray flux detected spectroscopically.

We ascribe the discrepancy of the image and spectrum to variability of NGC 6221 in the two years between these observations. The total flux, as well as the relative fractions of resolved and thermal emission are significantly different between the *ROSAT* and *ASCA* data sets, with greater flux measured by *ASCA*. The total observed HRI count rate is consistent with the *ASCA* flux due to only two of the three soft components of the spectral model: the thermal and scattered components. The relative contributions of these two components correspond to the extended and unresolved components of the image. The total flux measured with *ASCA* then includes an additional component, the weakly absorbed intrinsic AGN, which dominates the soft emission.

Flux variability may be due to a change in either the

AGN itself or the intrinsic column density between the *ROSAT* and *ASCA* observations. An increase in the AGN power by a factor of about 5 between the observations is consistent with the data. Alternatively, N_H may have diminished significantly. The intrinsic column density we fit to the 1997 data, $N_H = 1.1 \times 10^{22} \text{ cm}^{-2}$, is extremely low. If it had been more typical of the rest of the Sy2/SB sample, $N_H \approx 10^{23} \text{ cm}^{-2}$, at the time the *ROSAT* data were obtained, none of the *ROSAT*-detected flux would have been due to the intrinsic AGN. NGC 6221 is the host of SN1990W, a type Ib (Wheeler et al. 1994) supernova, but this is unlikely to be the source of X-ray variation or the extended emission.

5.12. NGC 7130

NGC 7130 is peculiar and contains a bar, detected at near-infrared wavelengths (Mulchaey et al. 1997).

The X-ray spectrum is best fit with a single power law and thermal emission. The latter dominates, accounting for 57% of the soft X-ray flux. In this model, the absorption on the power law is low, consistent with the Galactic value alone, which implies that we do not observe the buried AGN directly. The quality of these *ASCA* data is not extremely high, however. Although the complex model does not significantly improve the fit, it yields reasonable results. We find $N_H = 10^{24} \text{ cm}^{-2}$ and a scattered fraction $f_{scatt} = 0.01$ in this case, while the thermal contribution does not change.

We detect extended emission in the extremely short (5 ks) HRI exposure, with $R_{kpc} = 16$.

5.13. NGC 7582

NGC 7582 is a group member and contains a bar.

As mentioned above, medium energy emission from NGC 7582 varies (Xue et al. 1998), so we have treated the two *ASCA* observations separately and combined each with the single PSPC data set for the joint fits. In both cases, the best-fitting model includes a scattered power law, thermal emission, and a narrow line near 6.3 keV. We attribute the spectral variation to a change in absorbing column density. The intrinsic AGN is strong in NGC 7582, nearly $10^{-2} \text{ photons keV}^{-1} \text{ cm}^{-2} \text{ s}^{-1}$ at 1 keV. The intrinsic AGN thus contributes to the soft X-ray flux, so the thermal emission accounts for 0.16 and 0.28 of the total in the two observations.

The X-ray emission is extended, on scales of 3.1 and 5.1 kpc in the HRI and PSPC, respectively. The extended fraction is greater in the HRI observation (0.56), from 1995 May, than in the PSPC observation (0.38), taken in 1993 May. We also observe complex structure in this nearby galaxy, and differences between the hard and soft PSPC images.

The optical spectrum of NGC 7582 has varied in recent years, exhibiting broad lines as of July 1998. Aretxaga et al. (1999) discuss several possible causes for this transformation to an optical spectrum characteristic of a Seyfert 1 and favor the appearance of a Type II_n supernova in the starburst. These and other X-ray observations (Turner et al. 2000) suggest, however, that the column density that obscures the nucleus varies. Although a simple increase in extinction with the local reddening law is not consistent with the optical continuum variations, the contribution

of the starburst component may not be adequately distinguished in the present optical spectra (Aretxaga et al. 1999).

Discussed above (§3.2), the nearby companion, RX J231829.9-422041, is much fainter than NGC 7582, especially at harder energies. The spectrum of RX J231829.9-422041 is soft. We fit the PSPC spectrum of this source alone with a single power law, $\Gamma = 2.1(+0.44, -0.48)$ and Galactic absorption.

5.14. NGC 7674

NGC 7674 is interacting with UGC 12608, located 17 kpc (32'') toward the northeast. This galaxy exhibits broad lines in polarized light (Miller & Goodrich 1990; Tran 1995a).

NGC 7674 was observed with the PSPC for only 3 ks. The best fit to these limited data is a power law, with $\Gamma = 2.0(+0.72, -1.3)$. Although the measurement errors do not constrain the extended fraction of soft X-ray emission well, this galaxy is resolved, with $R_{kpc} = 45$.

6. CONCLUSIONS

In this work, we present the results of X-ray imaging and spectroscopy of a sample of Seyfert/starburst composite galaxies. These are active galaxies that also contain significant star formation. The sample is flux-limited, based on optical ([O III] $\lambda\lambda 4959 + 5007$) and radio (1.4 GHz) nuclear fluxes, and the starbursts are detected in optical and UV observations. Acknowledging the relevant physical processes of these galaxies, we find spatial and spectral evidence for both AGN and starburst activity in the sample members.

The *ROSAT* images of 85% of this sample of Seyfert/starburst composite galaxies reveal extended emission. In several cases, where the PSPC data are of extremely high quality, we also spatially differentiate soft and hard emission in broad X-ray bands. We expected that emission processes other than the AGNs would be important in these galaxies, for they were specifically selected to contain a circumnuclear starburst. By analogy with nearby starburst galaxies, we attribute the extended X-ray emission to thermal gas produced in a starburst-driven outflow.

We apply a consistent set of spectroscopic models to the X-ray emission, detected primarily with *ASCA* and supplemented by the *ROSAT* PSPC. All the *ASCA* spectra require models that are more complex than a single absorbed power law. This model deficiency is most apparent as a soft X-ray excess, a high excess of counts compared with extrapolation of the power law at low energies, in the residuals. Applying the progressively more complex models described above, we consistently identify the additional power law and thermal components in the present sample.

The principal components of the resultant best-fitting models are power laws, emission lines, and thermal emission. The power laws represent the underlying AGN and its scattered emission, although in many cases we do not detect the AGN directly because it is heavily absorbed by material in the galaxy. The emission lines, centered near 6.4 keV, are also due to the AGN. In most of our sample members, the lines are unresolved spectrally, which is typical in Sy 2s, where this emission originates some dis-

tance from the nucleus. With one exception (NGC 6221), all the AGNs are heavily-absorbed, with $N_H > 10^{23} \text{ cm}^{-2}$, and the strength of the Fe K lines are consistent with these column densities.

Thermal emission dominating at energies less than about 1 keV is the X-ray signature of the starburst. An outflowing superwind, powered by the stellar winds and supernovae of the starburst, are its immediate origin. Only in one case (Mrk 477) do we fail to detect significantly this starburst signature.

The imaging and spectroscopy results are generally consistent, supporting the association of the spatially extended and spectrally-identified thermal emission. Thus, we detect the starburst component of these composite galaxies in X-rays.

In Paper II, we apply the results obtained through the detailed data analysis of the present work and relate them to the larger issues of the Seyfert-starburst connection. We compare the X-ray characteristics of these Sy2/SB composites with “pure” starbursts and AGNs and illustrate

the composite nature of the Sy2/SBs at other wavelengths. We also identify the distinctive signatures of the various energy sources in these different types of galaxies using multi-wavelength diagnostics.

This work was supported by NASA grants NAG5-6917 and NAG5-6400. This research has made use of the NASA/IPAC Extragalactic Database (NED) which is operated by the Jet Propulsion Laboratory, California Institute of Technology, under contract with the National Aeronautics and Space Administration, the Astronomical Data Center at NASA Goddard Space Flight Center, and the High Energy Astrophysics Science Archive Research Center Online Service provided by the NASA Goddard Space Flight Center. The Digitized Sky Surveys were produced at the Space Telescope Science Institute under U.S. Government grant NAG W-2166. The images of these surveys are based on photographic data obtained using the Oschin Schmidt Telescope on Palomar Mountain and the UK Schmidt Telescope.

REFERENCES

- Antonucci, R. 1993, *ARA&A*, 31, 473
 Antonucci, R. R. J., & Miller, J. S. 1985, *ApJ*, 297, 621
 Aretxaga, L., Joguet, B., Kunth, D., Melnick, J., & Terlevich, R. J. 1999, *ApJ*, 519, L123
 Arnaud, M., & Rothenflug, M. 1985, *A&AS*, 60, 425
 Awaki, H., Koyama, K., Inoue, H., & Halpern, J. P. 1991, *PASJ*, 43, 195
 Boyle, B. J., & Terlevich, R. J. 1998, *MNRAS*, 293, L49
 Chevalier, R. A., & Clegg, A. W. 1985, *Nature*, 317, 44
 Cid Fernandes, R., Jr., & Terlevich, R. 1995, *MNRAS*, 272, 423
 Cid Fernandes, R., Jr., Storch-Bergmann, T., & Schmitt, H. R. 1998, *MNRAS*, 297, 579
 Dahlem, M., Weaver, K. A., & Heckman, T. M. 1998, *ApJS*, 118, 401
 David, L. P., Harnden, F. R., Kearns, K. E., & Zombeck, M. V. 1999, The ROSAT High Resolution Imager (HRI) Calibration Report (US ROSAT Science Data Center/SAO: Cambridge)
 Dickey, J. M., & Lockman, F. J. 1990, *ARA&A*, 28, 215
 Elvis, M., Lockman, F. J., & Wilkes, B. J. 1989, *AJ*, 97, 777
 Ferrarese, L., & Merritt, D. 2000, *ApJ*, 539, L9
 Garcia, A. M. 1993, *A&AS*, 100, 47
 Genzel, R., et al. 1998, *ApJ*, 498, 579
 Gebhardt, K., et al. 2000, *ApJ*, 539, L13
 Ghisellini, G., Haardt, F., & Matt, G. 1994, *MNRAS*, 267, 743
 González Delgado, R. M. et al. 1998, *ApJ*, 505, 174
 González Delgado, R. M., Heckman, T. M., & Leitherer, C. 2000, submitted to *ApJ*
 Hasinger, G., Turner, T. J., George, I. M., & Boese, G. 1992, *Legacy*, 2, 77
 Heckman, T. M., Lehnert, M., & Armus, L. 1993, in “The Environment and Evolution of Galaxies,” ed. Shull & Thronson (Kluwer: Dordrecht), 455
 Heckman, T. M. et al. 1995, *ApJ*, 452, 549
 Heckman, T. M. et al. 1997, *ApJ*, 482, 114
 Iwasawa, K., Fabian, A. C., & Matt, G. 1997, *MNRAS*, 289, 443
 Kaastra, J. S. 1992, “An X-Ray Spectral Code for Optically Thin Plasmas,” Internal SRON-Leiden Report
 Kollatschny, W., & Fricke, K. J. 1989, *A&A*, 219, 34
 Kollatschny, W., & Kowatsch, P. 1998, *A&A*, 336, L21
 Levenson, N. A., Weaver, K. A., & Heckman, T. M. 2000, submitted to *ApJ* (Paper II)
 Liedahl, D. A. 1992, Ph.D. Dissertation, University of California, Berkeley
 McKee, C. F., & Ostriker, J. P. 1977, *ApJ*, 218, 148
 Mewe, R., Gronenschild, E. H. B. M., & van den Oord, G. H. J. 1985, *A&AS*, 62, 197
 Mewe, R., Lemen, J. R., & van den Oord, G. H. J. 1986, *A&AS*, 65, 511
 Miller, J. S., & Goodrich, R. W. 1990, *ApJ*, 355, 456
 Miyoshi, M., Moran, J., Herrnstein, J., Greenhill, L., Nakai, N., Diamond, P., & Inoue, M. 1995, *Nature*, 373, 127
 Morse, J. A. 1994, *PASP*, 106, 675
 Mulchaey, J. S., Regan, M. W., & Kundu, A. 1997, *ApJS*, 110, 299
 Murphy, E. M., Lockman, F. J., Laor, A., & Elvis, M. 1996, *ApJS*, 105, 369
 Nandra, K., & Pounds, K. A. 1994, *MNRAS*, 268, 405
 Nandra, K., George, I. M., Mushotzky, R. F., Turner, T. J., & Yaqoob, T. 1997, *ApJ*, 477, 602
 Netzer, H., & Turner, T. J. 1997, *ApJ*, 488, 694
 Pedlar, A., Meaburn, J., Axon, D. J., Unger, S. W., Whittle, D. M., Meurs, E. J. A., Guerrine, N., & Ward, M. J. 1989, *MNRAS*, 238, 863
 Pence, W. D., & Blackman, C. P. 1984, *MNRAS*, 207, 9
 Schachter, J. F., et al. 1998, *ApJ*, 503, L126
 Schmitt, H. R., Kinney, A. L., Storch-Bergmann, T., & Antonucci, R. 1997, *ApJ*, 477, 623
 Schmitt, H. R., & Storch-Bergmann, T. 1995, *MNRAS*, 276, 592
 Schmitt, H. R., Storch-Bergmann, T., & Cid Fernandes, R. 1999, *MNRAS*, 303, 173
 Tanaka, Y., Holt, S. S., Inoue, I., & Holt, S. S., 1994, *PASJ*, 46, L37
 Tanaka, Y., et al. 1995, *Nature*, 375, 659
 Thronson, H. A., Jr., et al. 1989, *ApJ*, 343, 158
 Tran, H. D., Miller, J. S., & Kay, L. E. 1992, *ApJ*, 397, 452
 Tran, H. D. 1995a, *ApJ*, 440, 565
 Tran, H. D. 1995b, *ApJ*, 440, 578
 Tran, H. D. 1995c, *ApJ*, 440, 597
 Turner, T. J., George, I. M., Nandra, K., & Mushotzky, R. F. 1997, *ApJS*, 113, 23
 Turner, T. J., Perola, G. C., Fiore, F., Matt, G., George, I. M., Piro, L., & Bassani, L. 2000, *ApJ*, 531, 245
 Turner, T. J., Urry, C. M., & Mushotzky, R. F. 1993, *ApJ*, 418, 653
 Ueno, S., Mushotzky, R. F., Koyama, K., Iwasawa, K., Awaki, H., & Hayashi, I. 1994, *PASJ*, 46, L71
 Urry, C. M., & Padovani, P. 1995, *PASP*, 107, 803
 Veron, M. P., Veron, P., & Zuiderwijk, E. J. 1981, *A&A*, 98, 34
 Wang, J., Heckman, T. M., & Lehnert, M. D. 1997, *ApJ*, 491, 114
 Weaver, K. A., Nousek, J., Yaqoob, T., Mushotzky, R. F., Makino, F., & Otani, C. 1996, *ApJ*, 458, 160
 Weaver, K. A., Awaki, H., Muchaey, J. S., Colbert, E. J. M., Yaqoob, T., & Ueno, S. 2000, submitted to *ApJ*
 Weaver, K. A., Gelbord, J., & Yaqoob, T. 2000, submitted to *ApJ*
 Wheeler, J. C., Harkness, R. P., Clocchiatti, A., Benetti, S., Brotherton, M. S., Depoy, D. L., & Elias, J. 1994, *ApJ*, 436, L135
 Whittle, M. 1992, *ApJS*, 79, 49
 Wilson, A. S., Elvis, M., Lawrence, A., & Bland-Hawthorn, J. 1992, *ApJ*, 391, L75
 Wilson, A. S., & Ulvestad, J. S. 1982, *ApJ*, 263, 576
 Xue, S.-J., Otani, C., Mihara, T., Cappi, M., & Matsuoka, M. 1998, *PASJ*, 50, 519
 Zwicky, F. 1971, Catalog of Selected Compact Galaxies and Post-Eruptive Galaxies, Guemlingen, Switzerland

TABLE 1
BASIC PROPERTIES OF THE SELECTED GALAXIES

Galaxy	RA			DEC			D	Scale	Galactic N_H	i	References
	(h	m	s)	($^{\circ}$	'	"	(Mpc)	(pc/"	(10^{20} cm $^{-2}$)	($^{\circ}$)	
NGC 1068	02	42	40.71	-00	00	47.8	15.2	74	3.0	32	1, 4
Mrk 1066	02	59	58.59	+36	49	14.3	48	233	12	54	2, 4, 6
Mrk 1073	03	15	01.43	+42	02	09.4	93	452	1.1	42	2, 5, 6
Mrk 78	07	42	41.73	+65	10	37.5	149	720	4.1	60	2, 4, 6
IC 3639	12	40	52.88	-36	45	21.5	44	212	5.1	34	2, 5, 7
NGC 5135	13	25	43.97	-29	50	02.3	55	266	4.7	46	2, 4, 7, 8, 9
Mrk 266	13	38	17.69	+48	16	33.9	111	540	1.5	...	1, 4, 10
Mrk 273	13	44	42.11	+55	53	12.6	151	732	0.97	...	1, 5, 6
Mrk 463	13	56	02.87	+18	22	19.5	199	963	2.1	10	2, 5, 6
Mrk 477	14	40	38.11	+53	30	16.0	151	733	1.3	...	2, 5, 7, 11
NGC 6221	16	52	46.67	-59	12	59.0	20	96	15	43	2, 5, 8
NGC 7130	21	48	19.48	-34	57	09.2	65	313	2.0	29	2, 5, 7, 8, 9
NGC 7582	23	18	23.50	-42	22	14.0	21	102	1.5	62	3, 5, 8, 9
NGC 7674	23	27	56.72	+08	46	44.5	116	563	5.2	25	2, 4, 6

References. — (1) Murphy et al. (1996); (2) Dickey & Lockman (1990); (3) Elvis, Lockman, & Wilkes (1989); (4) Schmitt et al. (1997); (5) Whittle (1992); (6) Gonzalez-Delgado et al. (2000); (7) Gonzalez-Delgado et al. (1998); (8) Cid Fernandes et al. (1998); (9) Schmitt et al. (1999); (10) Wang et al. (1997); (11) Heckman et al. (1997)

TABLE 2
SEYFERT/STARBURST X-RAY OBSERVATIONS

Galaxy	HRI			PSPC			ASCA			SIS CCD Mode
	Date	Exposure (ks)	Rate (cts s ⁻¹)	Date	Exposure (ks)	Rate (cts s ⁻¹)	Date	Exposure ^a (ks)	Rate ^a (cts s ⁻¹)	
NGC 1068	1995 Jul	71.4	0.638	1993 Jul	5.30	1.562	1996 Aug	93.8	0.372	1
Mrk 1066	1996 Feb	15.4	0.004	1997 Aug	34.3	0.010	1
	1998 Jan	25.6	0.004	
Mrk 1073	1998 Aug	20.7	0.004	1999 Sep	25.7	0.012	1
Mrk 78	1996 Mar	16.7	0.004	1991 Mar	14.3	0.008
IC 3639	1998 Jan	39.1	0.005	1998 Jul	37.0	0.008	1
NGC 5135	1998 Jan	35.0	0.014	1992 Jul	9.24	0.040	1995 Jan	44.4	0.015	1
Mrk 266	1996 Jun	39.4	0.012	1991 Dec	9.54	0.032	1999 May	18.0	0.013	1
Mrk 273	1992 May	19.2	0.004	1992 Jun	19.9	0.010	1994 Dec	40.6	0.009	1
Mrk 463	1992 Jan	1.05	...	1992 Jan	11.1	0.017	1994 Jan	36.6	0.007	2
Mrk 477	1997 Dec	20.5	0.008	1995 Dec	26.7	0.012	1
	1995 Dec	17.1	0.012	1
NGC 6221	1995 Sep	11.9	0.033	1997 Sep	35.1	0.315	1
NGC 7130	1998 Apr	5.26	0.010	1996 Nov	35.9	0.013	1
NGC 7582	1995 May	17.3	0.015	1993 May	7.24	0.042	1994 Nov	20.2	0.087	2
	1996 Nov	37.1	0.115	1
NGC 7674	1992 Jun	0.89	...	1992 Dec	3.71	0.016

^aSIS0

Note. — Rates are background-subtracted.

TABLE 3
EXTENDED AND THERMAL SOFT X-RAY EMISSION

Galaxy	HRI			PSPC			ASCA
	R_{kpc}^a	f^b	f^c	R_{kpc}^a	f^b	f^c	f_{therm}^d
NGC 1068	7.4	$0.51^{+0.05}_{-0.09}$	0.73 ± 0.02	7.4	0.40 ± 0.02	0.60 ± 0.06	0.80
Mrk 1066	0.0	< 0.15	< 0.71	0.51
Mrk 1073	9.5	$0.53^{+0.18}_{-0.28}$	$0.84^{+0.16}_{-0.50}$	0.91
Mrk 78	17	$0.38^{+0.20}_{-0.30}$	$0.72^{+0.28}_{-0.54}$	36	< 0.62	$0.72^{+0.28}_{-0.45}$...
IC 3639	6.8	$0.39^{+0.11}_{-0.21}$	0.68 ± 0.31	1.00
NGC 5135	5.3	$0.46^{+0.06}_{-0.16}$	0.65 ± 0.20	13	$0.19^{+0.07}_{-0.11}$	< 0.32	0.54
Mrk 266	22	$0.78^{+0.06}_{-0.16}$	$0.92^{+0.08}_{-0.20}$	32	$0.49^{+0.08}_{-0.12}$	$0.77^{+0.23}_{-0.28}$	0.43
Mrk 273	18	< 0.39	$0.53^{+0.47}_{-0.49}$	37	< 0.28	< 0.62	0.43
Mrk 463	48	< 0.41	< 0.67	0.31
Mrk 477	15	< 0.30	0.54 ± 0.35	0.00
NGC 6221	4.8	$0.52^{+0.07}_{-0.17}$	$0.96^{+0.04}_{-0.22}$	0.05
NGC 7130	16	$0.44^{+0.23}_{-0.33}$	< 0.63	0.57
NGC 7582	3.1	$0.56^{+0.09}_{-0.19}$	$0.94^{+0.06}_{-0.27}$	5.1	$0.38^{+0.08}_{-0.12}$	0.54 ± 0.28	0.16, 0.28
NGC 7674	45	$0.65^{+0.48}_{-0.52}$	< 0.57	...

^aMaximum radius of extended emission (kpc).

^bMinimum extended fraction of total emission, with 90% confidence errors.

^cConstrained measurement of extended fraction of total emission.

^dThermal fraction of soft emission in spectrum.

TABLE 4
 POWER LAW MODELS

Galaxy	N^a_H	Γ^b	$A1^c$	F_{2-10}^d	$F_{0.5-2}^e$	χ^2/dof
<i>ASCA</i>						
NGC 1068	$3 :^{+0.1}_{-0}$	3.2 ± 0.02	40 ± 1.0	20 ± 0.5	86 ± 2.0	8533/813
Mrk 1066	$12 :^{+9.4}_{-0}$	1.8 ± 0.25	$0.91^{+0.22}_{-0.17}$	$2.9^{+0.45}_{-0.41}$	$1.4^{+0.22}_{-0.20}$	100/76
Mrk 1073	$1.4 :^{+13}_{-0}$	$1.2^{+0.38}_{-0.40}$	$0.61^{+0.26}_{-0.23}$	5.2 ± 1.0	1.3 ± 0.26	132/64
IC 3639	$5.0 :^{+20}_{-0}$	1.3 ± 0.4	$0.51^{+0.3}_{-0.2}$	$3.7^{+2.1}_{-1.6}$	$1.0^{+0.6}_{-0.4}$	64/54
NGC 5135	$4.7 :^{+4.4}_{-0}$	$3.0^{+0.3}_{-0.2}$	1.9 ± 0.4	1.4 ± 0.3	5.5 ± 1.0	215/100
Mrk 266	$1.5 :^{+10}_{-0}$	$2.2^{+0.6}_{-0.6}$	$1.1^{+0.7}_{-0.4}$	$2.0^{+1.0}_{-0.5}$	$2.2^{+1.1}_{-0.6}$	28/34
Mrk 273	$1.0 :^{+5.1}_{-0}$	$1.3^{+0.31}_{-0.32}$	$0.46^{+0.16}_{-0.14}$	$3.5^{+0.70}_{-0.46}$	$1.0^{+0.2}_{-0.13}$	123/61
Mrk 463	$2.0 :^{+7.5}_{-0}$	$0.65^{+0.24}_{-0.23}$	$0.27^{+0.094}_{-0.077}$	6.1 ± 1.2	0.64 ± 0.13	123/72
Mrk 477	$1.3 :^{+10}_{-0}$	0.12 ± 0.3	$0.22^{+0.2}_{-0.1}$	13 ± 1.4	0.62 ± 0.06	65/106
NGC 6221	$78^{+4.9}_{-4.7}$	1.7 ± 0.05	$38^{+2.7}_{-2.5}$	140 ± 7.0	24 ± 1.2	846/769
NGC 7130	$2.0 :^{+20}_{-0}$	$2.6^{+0.7}_{-0.3}$	$1.2^{+0.7}_{-0.4}$	$2.4^{+1.6}_{-0.8}$	$2.4^{+1.6}_{-0.8}$	103/75
NGC 7582 (1994)	520^{+120}_{-70}	$1.0^{+0.3}_{-0.2}$	$16^{+9.8}_{-4.1}$	160 ± 7.0	$34^{+1.5}_{-1.4}$	527/286
NGC 7582 (1996)	760^{+72}_{-90}	$1.1^{+0.1}_{-0.2}$	21 ± 7.5	160 ± 32	0.26 ± 0.1	1614/469
<i>ASCA + PSPC</i>						
NGC 1068	4.6 ± 0.2	3.3 ± 0.03	42 ± 11	19 ± 0.4	85 ± 1.6	8975/936
NGC 5135	$8.0^{+2.3}_{-1.6}$	$3.2^{+0.3}_{-0.2}$	$2.1^{+0.5}_{-0.4}$	1.0 ± 0.2	3.6 ± 0.6	242/121
Mrk 266	$3.7^{+2.4}_{-1.5}$	$2.7^{+0.6}_{-0.5}$	$1.2^{+0.3}_{-0.2}$	1.2 ± 0.2	2.4 ± 0.4	64/51
Mrk 273	$2.2^{+2.1}_{-1.2}$	$1.4^{+0.24}_{-0.22}$	$0.51^{+0.085}_{-0.11}$	$3.4^{+0.41}_{-0.58}$	$1.0^{+0.12}_{-0.17}$	151/72
Mrk 463	$2.0 :^{+1.8}_{-0}$	$0.78^{+0.23}_{-0.22}$	$0.30^{+0.076}_{-0.066}$	$5.6^{+1.1}_{-0.95}$	$0.65^{+1.2}_{-1.1}$	168/89
NGC 7582 (1994)	520^{+80}_{-110}	$1.1^{+0.2}_{-0.3}$	$18^{+6.9}_{-6.7}$	$160^{+7.1}_{-6.9}$	$0.77^{+0.04}_{-0.03}$	795/302
NGC 7582 (1996)	740 ± 80	1.1 ± 0.1	20 ± 7.8	160 ± 32	0.26 ± 0.1	1861/484

^aColumn density in units of 10^{20} cm^{-2} .

^bPhoton index of power law.

^cNormalization of power law in units of $10^{-4} \text{ photons keV}^{-1} \text{ cm}^{-2} \text{ s}^{-1}$ at 1 keV.

^d2.0–10.0 keV model flux in SIS0 detector in units of $10^{-13} \text{ erg cm}^{-2} \text{ s}^{-1}$.

^e0.5–2.0 keV model flux in SIS0 detector in units of $10^{-13} \text{ erg cm}^{-2} \text{ s}^{-1}$.

Note. — Errors are 90% confidence limits for two interesting parameters, except fluxes, where errors are 90% confidence for one parameter. Parameters that are constrained by hard limits are marked with a colon.

TABLE 5
SCATTERED POWER LAW MODELS ($\Gamma = 1.9$)

Galaxy	Hard Component			Soft Component		χ^2/dof
	N_H	A_1	F_{2-10}	A_2^a	$F_{0.5-2}$	
<i>ASCA</i>						
NGC 1068	3^{+2}_{-0}	$20^{+0.5}_{-5.7}$	$59^{+1.2}_{-18}$	0^{+64}_{-0}	$40.0^{+0.8}_{-12}$	24682/813
Mrk 1066	17100^{+32000}_{-5600}	38^{+180}_{-34}	6.1 ± 0.52	0.94 ± 0.10	1.5 ± 0.13	85/76
Mrk 1073	11500^{+15000}_{-4200}	32^{+89}_{-26}	9.3 ± 1.4	$0.98^{+0.19}_{-0.20}$	2.0 ± 0.30	118/64
IC 3639	3200^{+4600}_{-2000}	$3.4^{+6.0}_{-2.1}$	$5.1^{+1.8}_{-1.7}$	0.73 ± 0.25	1.4 ± 0.2	52/54
NGC 5135	22700^{+38000}_{-8900}	120^{+20000}_{-110}	$8.3^{+2.5}_{-2.4}$	$1.1^{+0.24}_{-0.17}$	$2.1^{+0.2}_{-0.1}$	310/100
Mrk 266	3300^{+1E+08}_{-3300}	$2.8^{+22}_{-2.8}$	4.9 ± 1.2	$0.89^{+0.31}_{-0.32}$	1.8 ± 0.5	25/34
Mrk 273	5300^{+3600}_{-1800}	$7.9^{+7.4}_{-3.8}$	6.3 ± 1.3	$0.67^{+0.068}_{-0.12}$	$1.4^{+0.095}_{-0.19}$	68/61
Mrk 463	3300^{+1700}_{-1200}	$6.5^{+6.7}_{-3.1}$	6.8 ± 1.4	$0.52^{+0.060}_{-0.095}$	$1.0^{+0.080}_{-0.15}$	88/72
Mrk 477	3220^{+1900}_{-1200}	$13^{+7.6}_{-5.9}$	13 ± 2.0	$0.62^{+0.21}_{-0.22}$	$1.2^{+0.1}_{-0.2}$	41/106
NGC 6221	$110^{+7.0}_{-6.7}$	45 ± 1.5	130 ± 2.7	$4.3^{+1.0}_{-1.1}$	24 ± 0.5	846/769
NGC 7130	36000^{+1E+08}_{-36000}	330^{+4700}_{-330}	$5.3^{+7.0}_{-5.0}$	$0.86^{+0.35}_{-0.22}$	$1.9^{+0.3}_{-0.04}$	126/75
NGC 7582 (1994)	1100^{+80}_{-70}	$87^{+6.3}_{-6.0}$	140 ± 6.3	$2.1^{+0.29}_{-0.33}$	$4.5^{+0.4}_{-0.6}$	357/286
NGC 7582 (1996)	1500 ± 50	$97^{+4.6}_{-4.5}$	140 ± 4.2	$2.1^{+0.14}_{-0.17}$	$4.4^{+0.2}_{-0.3}$	552/469
<i>ASCA + PSPC</i>						
NGC 1068	3^{+4E-03}_{-0}	$20^{+0.5}_{-2.3}$	$59^{+1.1}_{-3.2}$	$0.0^{+2.6}_{-0}$	$40^{+0.7}_{-2.2}$	27845/936
NGC 5135	22600^{+34000}_{-7300}	120^{+260}_{-110}	$8.2^{+2.9}_{-2.4}$	$1.1^{+0.22}_{-0.18}$	$2.1^{+0.3}_{-0.2}$	368/121
Mrk 266	3470^{+1E+08}_{-3500}	$2.6^{+4.2}_{-2.6}$	4.6 ± 0.6	$0.90^{+0.12}_{-0.13}$	1.8 ± 0.2	72/51
Mrk 273	5300^{+3500}_{-1600}	$7.8^{+7.5}_{-3.7}$	6.2 ± 1.2	$0.64^{+0.079}_{-0.073}$	$1.3^{+0.12}_{-0.25}$	131/72
Mrk 463	3300^{+1700}_{-990}	$6.5^{+6.0}_{-3.2}$	6.8 ± 1.4	$0.50^{+0.069}_{-0.059}$	$0.95^{+0.10}_{-0.084}$	109/89
NGC 7582 (1994)	1100^{+80}_{-70}	$87^{+6.2}_{-6.0}$	$140^{+1.8}_{-10}$	$2.1^{+0.27}_{-0.21}$	$4.0^{+0.4}_{-0.3}$	397/300
NGC 7582 (1996)	1500^{+57}_{-55}	$97^{+3.4}_{-3.3}$	140 ± 2.2	$2.1^{+0.12}_{-0.15}$	$4.2^{+0.15}_{-0.20}$	594/483

^aNormalization of the soft power-law component in units of 10^{-4} photons $\text{keV}^{-1} \text{cm}^{-2} \text{s}^{-1}$ at 1 keV.

Note. — Power law photon index is fixed at 1.9. Other symbols and errors are described in Notes to Table 4

TABLE 6
POWER LAW + THERMAL MODELS ($\Gamma = 1.9$)

Galaxy	Hard Component			Soft Component			χ^2/dof
	N_H	A1	F_{2-10}	kT^a	A3 ^b	$F_{0.5-2}$	
<i>ASCA</i>							
NGC 1068	$3^{+0.2}_{-0}$	12 ± 0.3	$37^{+0.6}_{-0.8}$	0.68 ± 0.01	$19^{+0.50}_{-0.55}$	$67^{+1.2}_{-1.4}$	4214/812
Mrk 1066	75^{+69}_{-46}	$1.1^{+0.23}_{-0.29}$	$3.0^{+0.48}_{-0.65}$	$0.88^{+0.23}_{-0.24}$	0.45 ± 0.26	$1.3^{+0.21}_{-0.29}$	90/75
Mrk 1073	400^{+390}_{-220}	$2.2^{+0.89}_{-0.70}$	$4.7^{+0.74}_{-0.85}$	$1.0^{+0.47}_{-0.29}$	$0.70^{+0.82}_{-0.28}$	1.3 ± 0.26	119/63
IC 3639	2100^{+3000}_{-1300}	$3.4^{+3.2}_{-1.7}$	4.8 ± 1.2	$2.3^{+2.9}_{-0.7}$	1.7 ± 0.53	1.2 ± 0.29	48/53
NGC 5135	4.7^{+20}_{-0}	0.71 ± 0.2	2.2 ± 0.2	$0.75^{+0.09}_{-0.1}$	0.78 ± 0.19	2.9 ± 0.3	154/99
Mrk 266	160^{+330}_{-150}	$1.2^{+1.1}_{-0.6}$	3.1 ± 1.1	0.78 ± 0.3	$0.73^{+0.35}_{-0.39}$	1.8 ± 0.6	13/33
Mrk 273	4200^{+2900}_{-1500}	$6.6^{+5.5}_{-2.4}$	5.8 ± 1.2	$3.2^{+2.2}_{-1.0}$	$1.7^{+0.27}_{-0.30}$	$1.2^{+0.14}_{-0.16}$	68/60
Mrk 463	3400^{+3500}_{-730}	$6.8^{+8.8}_{-3.5}$	7.1 ± 1.4	$5.7^{+24}_{-2.9}$	$1.5^{+0.70}_{-0.25}$	$0.84^{+0.17}_{-0.11}$	88/71
Mrk 477	3700^{+3800}_{-1600}	$14^{+20}_{-6.5}$	13 ± 2.3	$9.0^{+91}_{-6.2}$	$1.9^{+2.1}_{-0.70}$	1.1 ± 0.2	41/105
NGC 6221	$100^{+7.6}_{-4.5}$	$39^{+2.6}_{-2.5}$	140 ± 6.7	74^{+26}_{-62}	$25^{+6.5}_{-8.2}$	24 ± 1.2	832/768
NGC 7130	16^{+62}_{-14}	0.60 ± 0.3	1.8 ± 0.3	$0.79^{+0.2}_{-0.1}$	$0.56^{+0.29}_{-0.25}$	$2.0^{+0.3}_{-0.4}$	74/74
NGC 7582 (1994)	1130^{+50}_{-90}	$87^{+6.6}_{-6.9}$	140 ± 6.5	$13^{+87}_{-8.9}$	$7.1^{+5.0}_{-1.7}$	$3.9^{+0.5}_{-0.4}$	360/285
NGC 7582 (1996)	1480^{+70}_{-60}	$97^{+4.7}_{-4.6}$	140 ± 4.3	$6.4^{+5.6}_{-2.0}$	$6.3^{+0.79}_{-0.64}$	3.9 ± 0.2	572/468
<i>ASCA + PSPC</i>							
NGC 1068	$3^{+0.01}_{-0}$	12 ± 0.3	38 ± 0.7	0.67 ± 0.01	$19^{+0.53}_{-0.51}$	67 ± 1.3	7361/935
NGC 5135	$4.7^{+1.6}_{-0}$	0.74 ± 0.2	2.2 ± 0.2	$0.73^{+0.1}_{-0.2}$	$0.75^{+0.24}_{-0.21}$	2.9 ± 0.3	194/120
Mrk 266	$1.5^{+1.1}_{-0}$	0.75 ± 0.2	$2.1^{+0.4}_{-0.8}$	$0.28^{+0.1}_{-0.05}$	$0.72^{+0.42}_{-0.33}$	$2.6^{+0.5}_{-0.9}$	43/50
Mrk 273	4000^{+3100}_{-1500}	$6.4^{+5.9}_{-2.5}$	5.7 ± 1.1	$2.9^{+2.1}_{-0.83}$	$1.7^{+0.27}_{-0.32}$	$1.2^{+0.12}_{-0.15}$	96/71
Mrk 463	3100^{+2600}_{-1200}	$5.9^{+6.6}_{-2.6}$	6.5 ± 1.3	$4.3^{+7.4}_{-2.0}$	$1.4^{+0.25}_{-0.28}$	$0.85^{+0.11}_{-0.13}$	119/88
NGC 7582 (1994)	940 ± 60	$83^{+5.8}_{-5.6}$	140 ± 5.9	$1.0^{+0.1}_{-0.2}$	$1.6^{+0.34}_{-0.36}$	3.1 ± 0.4	455/299
NGC 7582 (1996)	1300^{+46}_{-48}	94 ± 3.2	140 ± 2.1	$0.56^{+0.059}_{-0.047}$	$17^{+3.7}_{-3.5}$	$3.4^{+0.28}_{-0.26}$	700/482

^aTemperature of thermal plasma in keV.

^bNormalization of thermal component in units of $10^{-4} \times K$, where $K = (10^{-14}/(4\pi D^2)) \int n_e n_H dV$, D is the distance to the source (cm), n_e is the electron density (cm^{-3}), and n_H is the hydrogen density (cm^{-2}).

Note. — Power law photon index is fixed at 1.9. Other symbols and errors are described in Notes to Table 4.

TABLE 7
SCATTERED POWER LAW + THERMAL MODELS ($\Gamma = 1.9$)

Galaxy	Hard Component			Soft Component				χ^2/dof
	N_H	$A1$	F_{2-10}	$A2$	kT	$A3$	$F_{0.5-2}$	
<i>ASCA</i>								
NGC 1068	9900^{+1000}_{-970}	86^{+18}_{-15}	58 ± 3.3	$11^{+0.28}_{-0.29}$	$0.69^{+0.01}_{-0.003}$	2.0 ± 0.53	66 ± 2.3	3363/811
Mrk 1066	14700^{+28500}_{-9000}	26^{+2000}_{-23}	$5.6^{+0.67}_{-0.78}$	$0.82^{+0.13}_{-0.15}$	$0.90^{+0.90}_{-0.66}$	$0.17^{+0.28}_{-0.15}$	$1.5^{+0.18}_{-0.21}$	79/74
NGC 5135	12900^{+16000}_{-6800}	25.7^{+120}_{-18}	$6.2^{+1.5}_{-1.6}$	$0.67^{+0.09}_{-0.15}$	$0.77^{+0.04}_{-0.1}$	$0.79^{+0.28}_{-0.14}$	$2.8^{+0.5}_{-0.2}$	108/98
Mrk 273	4500^{+2200}_{-1200}	$6.7^{+5.3}_{-3.0}$	5.6 ± 1.1	$0.49^{+0.16}_{-0.33}$	$1.1^{+1.8}_{-0.89}$	$0.20^{+0.28}_{-0.19}$	1.2 ± 0.24	62/59
Mrk 463	2900^{+1700}_{-1200}	$6.0^{+4.7}_{-2.8}$	6.6 ± 1.3	$0.40^{+0.080}_{-0.086}$	$0.71^{+0.53}_{-0.45}$	$0.15^{+0.080}_{-0.11}$	1.1 ± 0.17	80/70
<i>ASCA + PSPC</i>								
NGC 1068	3^{+10}_{-0}	$12^{+0.3}_{-1.7}$	$40^{+0.7}_{-0.6}$	$0^{+5.8}_{-0}$	0.67 ± 0.01	$1.9^{+5.2}_{-5.1}$	$66^{+1.3}_{-1.2}$	3363/811
NGC 5135	14000^{+16000}_{-3700}	29^{+100}_{-21}	6.3 ± 0.63	$0.71^{+0.11}_{-0.10}$	$0.68^{+0.14}_{-0.06}$	$0.79^{+0.10}_{-0.11}$	2.9 ± 0.29	150/119
Mrk 273	3600^{+2000}_{-1100}	$5.3^{+3.7}_{-2.0}$	5.3 ± 0.89	$0.38^{+0.085}_{-0.097}$	$0.83^{+0.49}_{-0.26}$	$0.28^{+0.090}_{-0.097}$	$1.3^{+0.21}_{-0.23}$	98/70
Mrk 463	2800^{+1300}_{-850}	$5.8^{+5.0}_{-2.7}$	6.6 ± 1.3	$0.40^{+0.085}_{-0.094}$	$0.66^{+0.35}_{-0.39}$	$0.16^{+0.086}_{-0.084}$	1.1 ± 0.17	96/87
NGC 7582 (1994)	1100^{+84}_{-76}	$86^{+5.4}_{-5.0}$	$140^{+4.1}_{-4.2}$	$1.9^{+0.26}_{-0.52}$	$0.37^{+0.30}_{-0.14}$	$0.63^{+0.64}_{-0.35}$	$4.7^{+0.37}_{-0.80}$	377/298
NGC 7582 (1996)	1400^{+58}_{-51}	$96^{+3.4}_{-3.3}$	$150^{+2.4}_{-2.6}$	$1.9^{+0.20}_{-0.16}$	$0.59^{+0.25}_{-0.30}$	$0.27^{+0.18}_{-0.13}$	$4.3^{+0.23}_{-0.22}$	575/481

Note. — Power law photon index is fixed at 1.9. Symbols and errors are described in Notes to Tables 4–6.

TABLE 8
BEST-FITTING MODELS ($\Gamma = 1.9$)

Galaxy	Hard Component						Soft Component						χ^2/dof
	N_H	$A1$	E_{line}^a	σ_{line}^b	EW_{line}^c	F_{2-10}	N_H	$A2$	kT	$A3$	$F_{0.5-2}$		
<i>ASCA</i>													
NGC 1068	$6.4^{+0.03}_{-0.06}$	0.05f	1000^{+260}_{-630}	49 ± 1.7	3.0f	$9.0^{+0.50}_{-0.56}$	0.69 ± 0.02	$18^{+0.39}_{-0.77}$	64.2 ± 3.2	1870/786	
	$6.6^{+0.07}_{-0.06}$	0.50f	4200^{+500}_{-630}	1.66 ± 0.2	$7.6^{+1.6}_{-1.3}$	
	$6.7^{+0.24}_{-0.08}$	0.05f	350^{+150}_{-190}	
Mrk 1066	57^{+59}_{-45}	$0.97^{+0.25}_{-0.29}$	$6.6^{+0.20}_{-0.52}$	0.05f	3200 ± 1900	3.6 ± 0.47	12f	...	$0.88^{+0.22}_{-0.20}$	$0.42^{+0.14}_{-0.11}$	1.3 ± 0.17	74/73	
Mrk 1073	400^{+390}_{-220}	$2.2^{+0.89}_{-0.70}$	$4.7^{+0.74}_{-0.85}$	14f	...	$1.0^{+0.47}_{-0.29}$	$0.70^{+0.82}_{-0.28}$	1.3 ± 0.26	119/63	
IC 3639	2100^{+3000}_{-1300}	$3.4^{+3.2}_{-1.7}$	< 830	4.8 ± 1.2	5.1f	...	$2.3^{+2.9}_{-0.7}$	1.7 ± 0.53	1.2 ± 0.29	48/53	
NGC 5135	12900^{+16000}_{-6800}	26^{+120}_{-18}	< 1100	$6.2^{+1.5}_{-1.6}$	4.7f	$0.67^{+0.09}_{-0.15}$	$0.77^{+0.04}_{-0.1}$	$0.79^{+0.28}_{-0.14}$	$2.8^{+0.5}_{-0.2}$	108/98	
Mrk 266	160^{+330}_{-150}	$1.2^{+1.1}_{-0.6}$	< 10000	3.1 ± 1.1	1.5f	...	0.78 ± 0.3	$0.73^{+0.35}_{-0.39}$	1.8 ± 0.6	13/33	
Mrk 273	3300^{+2900}_{-1100}	$3.9^{+2.3}_{-1.9}$	$6.5^{+0.21}_{-0.21}$	0.05f	860^{+130}_{-230}	5.2 ± 1.0	1.0f	$0.48^{+0.14}_{-0.21}$	$1.1^{+0.88}_{-0.77}$	$0.19^{+0.41}_{-0.17}$	1.2 ± 0.24	55/57	
Mrk 463	2900^{+1700}_{-1200}	$6.0^{+4.7}_{-2.8}$	< 890	6.6 ± 1.3	2.1f	$0.40^{+0.080}_{-0.086}$	$0.71^{+0.53}_{-0.45}$	$0.15^{+0.080}_{-0.11}$	1.1 ± 0.17	80/70	
Mrk 477	2400^{+1700}_{-1200}	$8.8^{+8.9}_{-4.3}$	$6.4^{+0.23}_{-0.21}$	0.05f	560^{+560}_{-500}	$12^{+2.3}_{-1.9}$	1.3f	$0.59^{+0.22}_{-0.20}$	1.2 ± 0.2	36/104	
NGC 6221	$110^{+8.6}_{-8.3}$	$46^{+1.9}_{-1.3}$	$6.6^{+0.31}_{-0.29}$	0.50f	360^{+210}_{-93}	140 ± 4.1	15f	$3.0^{+1.4}_{-1.5}$	$1.4^{+1.6}_{-0.5}$	$1.2^{+1.7}_{-0.69}$	24 ± 0.7	799/765	
NGC 7130	16^{+62}_{-14}	0.60 ± 0.3	< 5400	1.8 ± 0.3	2.0f	...	$0.79^{+0.2}_{-0.1}$	$0.56^{+0.29}_{-0.25}$	$2.0^{+0.3}_{-0.4}$	74/74	
NGC 7582 (1994)	1100^{+74}_{-78}	$84^{+6.6}_{-6.5}$	$6.2^{+0.17}_{-0.33}$	0.05f	190^{+60}_{-140}	140 ± 7.1	1.5f	$2.0^{+0.33}_{-0.30}$	$4.4^{+0.6}_{-0.5}$	344/284	
NGC 7582 (1996)	1400^{+60}_{-50}	$93^{+4.6}_{-4.4}$	6.3 ± 0.08	0.05f	150^{+53}_{-51}	140 ± 4.2	1.5f	$2.1^{+0.14}_{-0.16}$	$4.4^{+0.2}_{-0.3}$	516/467	
<i>ASCA + PSPC</i>													
NGC 1068	6.4 ± 0.05	0.05f	1000 ± 310	50 ± 2.5	3.0f	$11^{+0.27}_{-0.29}$	0.79 ± 0.01	$18^{+0.55}_{-0.46}$	100 ± 5.0	2315/910	
	6.6 ± 0.07	0.50f	3500^{+250}_{-390}	0.13 ± 0.005	$110^{+9.2}_{-7.9}$	
	$6.7^{+0.10}_{-0.14}$	0.05f	530^{+410}_{-280}	
NGC 5135	14000^{+16000}_{-3700}	29^{+100}_{-21}	< 590	6.3 ± 0.63	4.7f	$0.71^{+0.11}_{-0.10}$	$0.68^{+0.14}_{-0.06}$	$0.79^{+0.10}_{-0.11}$	2.9 ± 0.29	150/119	
Mrk 266	$1.5^{+1.1}_{-0}$	0.75 ± 0.2	< 9400	$2.1^{+0.4}_{-0.8}$	1.5f	...	$0.28^{+0.1}_{-0.05}$	$0.72^{+0.42}_{-0.33}$	$2.6^{+0.5}_{-0.9}$	43/50	
Mrk 273	2500^{+1500}_{-890}	$3.2^{+2.9}_{-1.4}$	$6.5^{+0.21}_{-0.17}$	0.05f	970^{+630}_{-680}	4.8 ± 0.91	1.0f	$0.35^{+0.082}_{-0.097}$	$0.84^{+0.48}_{-0.24}$	$0.28^{+0.17}_{-0.097}$	$1.3^{+0.15}_{-0.19}$	90/68	
Mrk 463	2800^{+1300}_{-850}	$5.8^{+5.0}_{-2.7}$	< 960	6.6 ± 1.3	2.1f	$0.40^{+0.085}_{-0.094}$	$0.66^{+0.35}_{-0.39}$	$0.16^{+0.086}_{-0.084}$	1.1 ± 0.17	96/87	
NGC 7582 (1994)	1000 ± 70	$84^{+6.4}_{-5.9}$	$6.2^{+0.18}_{-0.36}$	0.05f	160^{+100}_{-84}	$140^{+6.9}_{-6.1}$	$5.3^{+5.7}_{-1.6}$	$1.5^{+0.44}_{-0.32}$	$0.46^{+0.32}_{-0.19}$	$0.56^{+0.61}_{-0.32}$	$4.10^{+0.9}_{-1.0}$	365/297	
NGC 7582 (1996)	1400 ± 50	$93^{+4.6}_{-4.2}$	6.3 ± 0.08	0.05f	140^{+55}_{-48}	$140^{+4.3}_{-4.0}$	$5.6^{+3.4}_{-1.4}$	1.9 ± 0.20	$0.60^{+0.24}_{-0.30}$	$0.32^{+0.16}_{-0.17}$	4.2 ± 0.4	538/480	

^aEnergy of line center in keV.

^bLine width in keV.

^cEquivalent width of line in eV.

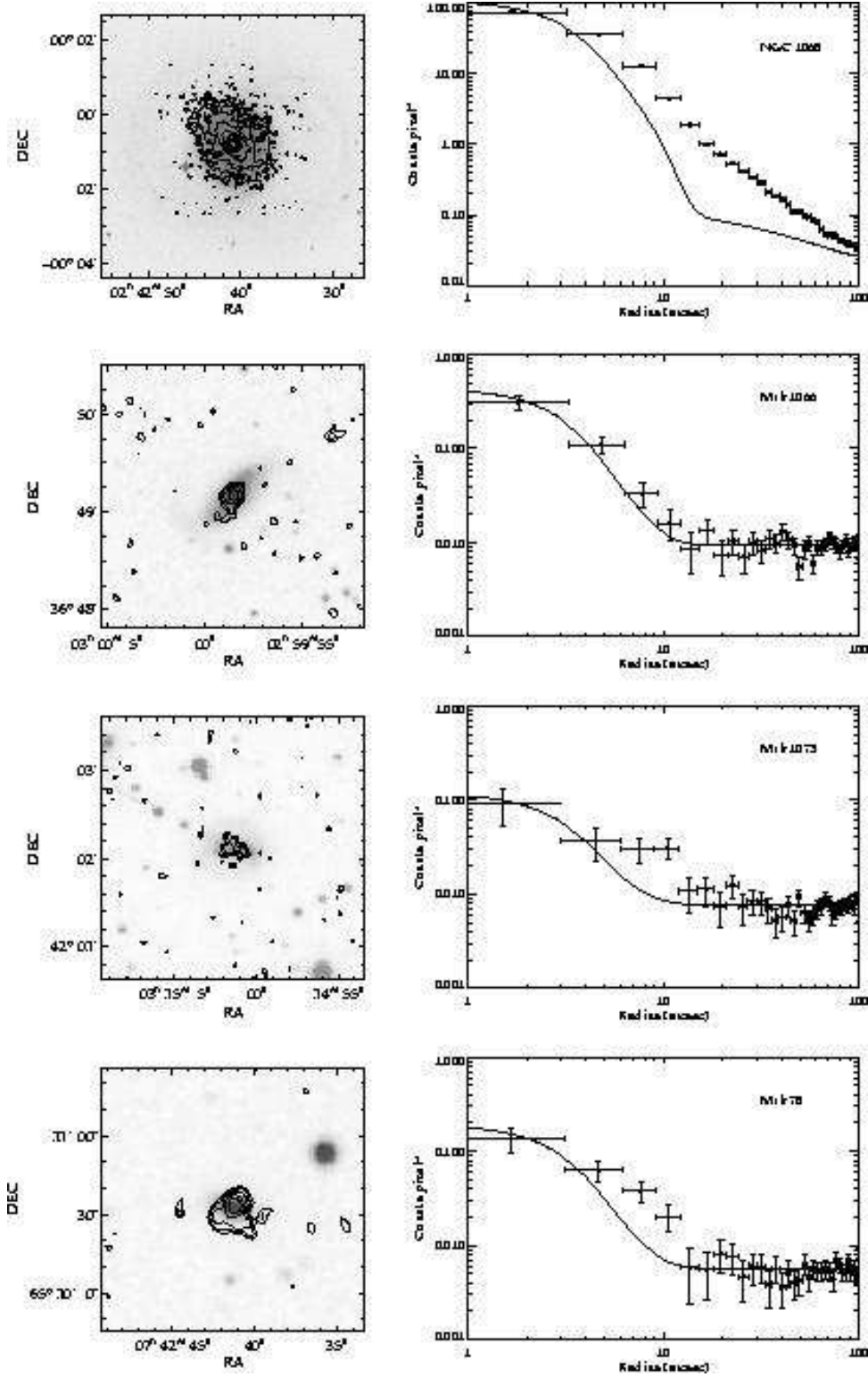
Note. — Power law photon index is fixed at 1.9. Additional fixed parameters are marked with f. Other symbols and errors are described in Notes to Tables 4–6.

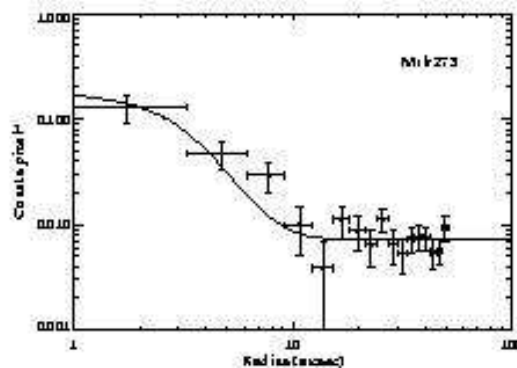
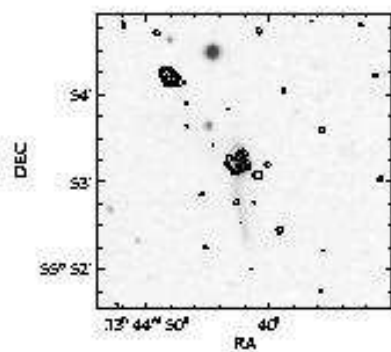
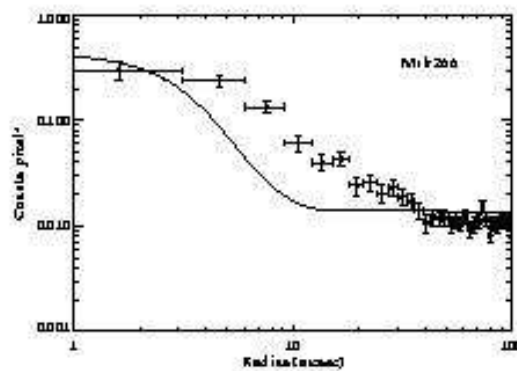
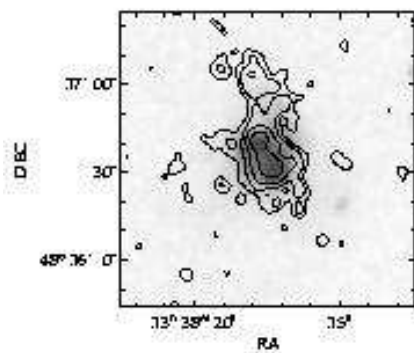
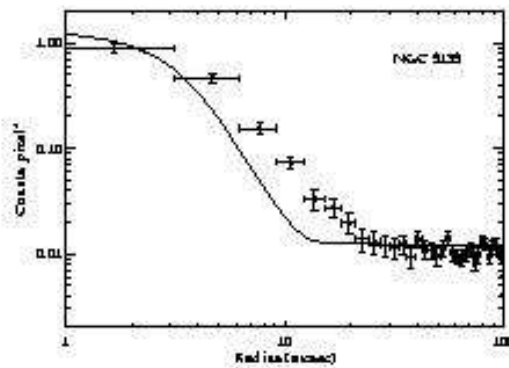
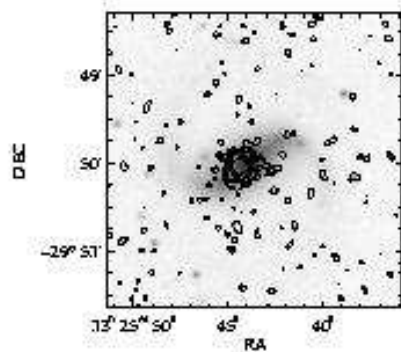
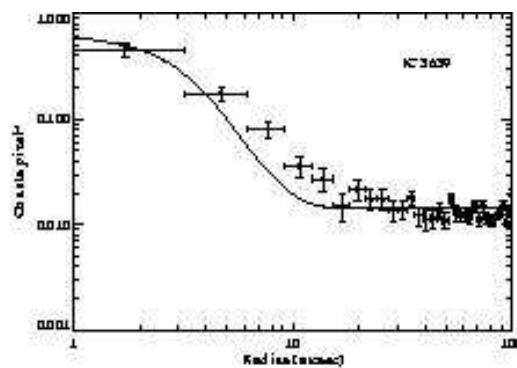
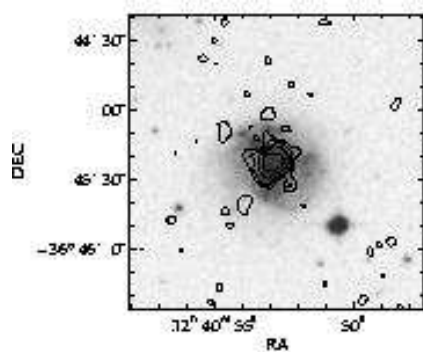
TABLE 9
SPECTRAL FITS TO PSPC DATA

Galaxy	kT or Γ	A^a	$F_{0.5-2}$	χ^2/dof
Mrk 78	$kT = 0.76 \pm 0.3$	3.2 ± 1.0	$0.060^{+0.1}_{-0.2}$	16/7
NGC 7674	$\Gamma = 2.0^{+0.6}_{-2.0}$	$1.3^{+6.8}_{-5.4}$	$2.3^{+1.0}_{-0.7}$	3/2

^aNormalization in units of 10^{-4} .

Note. — Column density is fixed at Galactic value. Other symbols and errors are described in Notes to Tables 4 and 6.





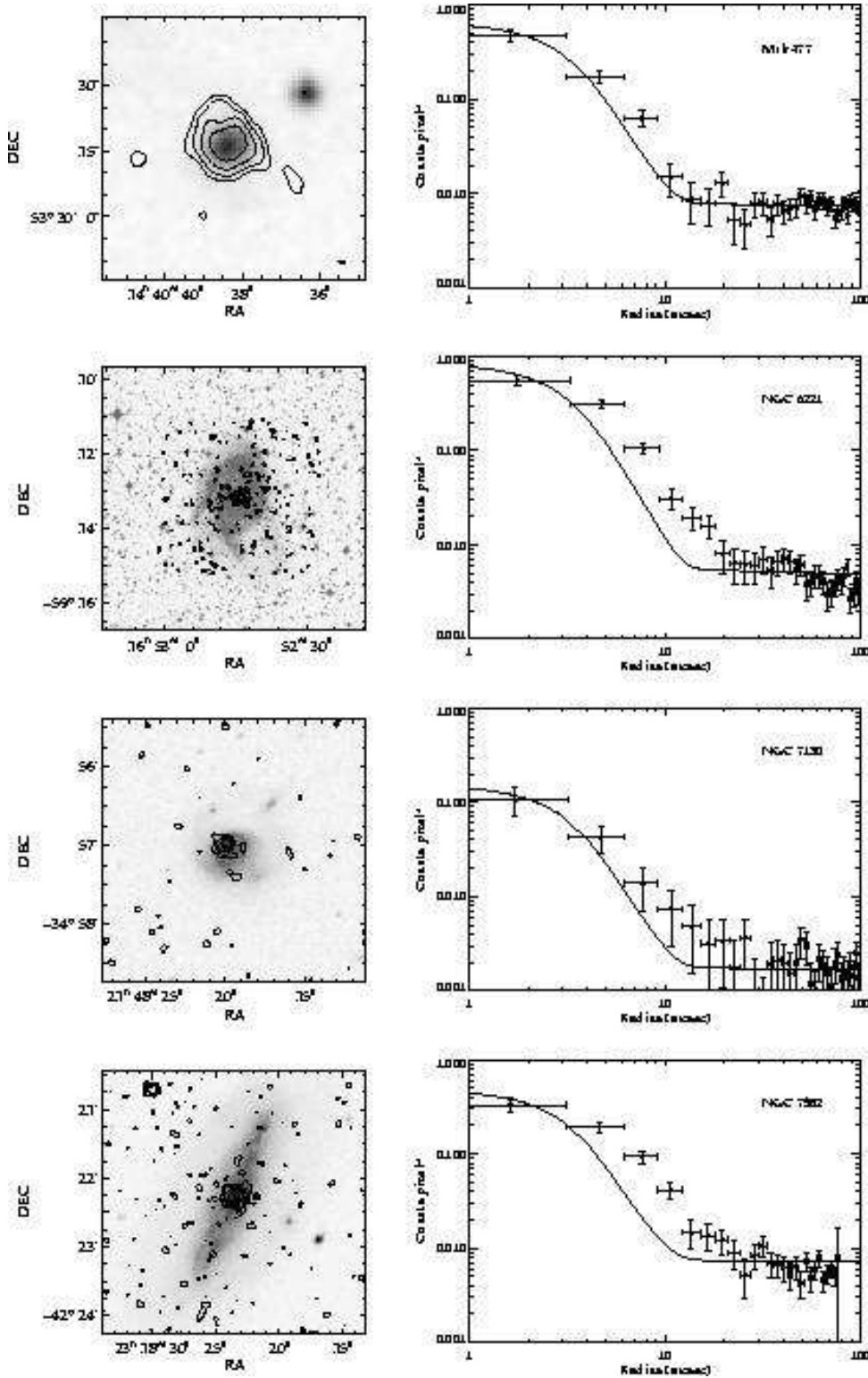


FIG. 1.— Contours of *ROSAT* HRI intensity overlaid on DSS images and radial profiles of HRI soft X-ray emission for the Sy2/SB sample. Raw X-ray data have been smoothed by a Gaussian of FWHM=4". The minimum contour level is 3 standard deviations above the background, and contour intervals are logarithmic, in factors of 2, except where noted. Radial profile data points are azimuthal averages of counts per raw (0".5) pixel. The background and amplitude are fit to the theoretical point-spread function (*solid line*). NGC 1068, with scale factor 3 in contour levels; Mrk 1066; Mrk 1073, scale factor 1.5; Mrk 78, scale factor 1.5; IC 3639; NGC 5135; Mrk 266; Mrk 273; Mrk 477, with minimum contour level 4σ ; NGC 6221; NGC 7130, minimum contour level 5σ ; NGC 7582, minimum contour level 3.5σ .

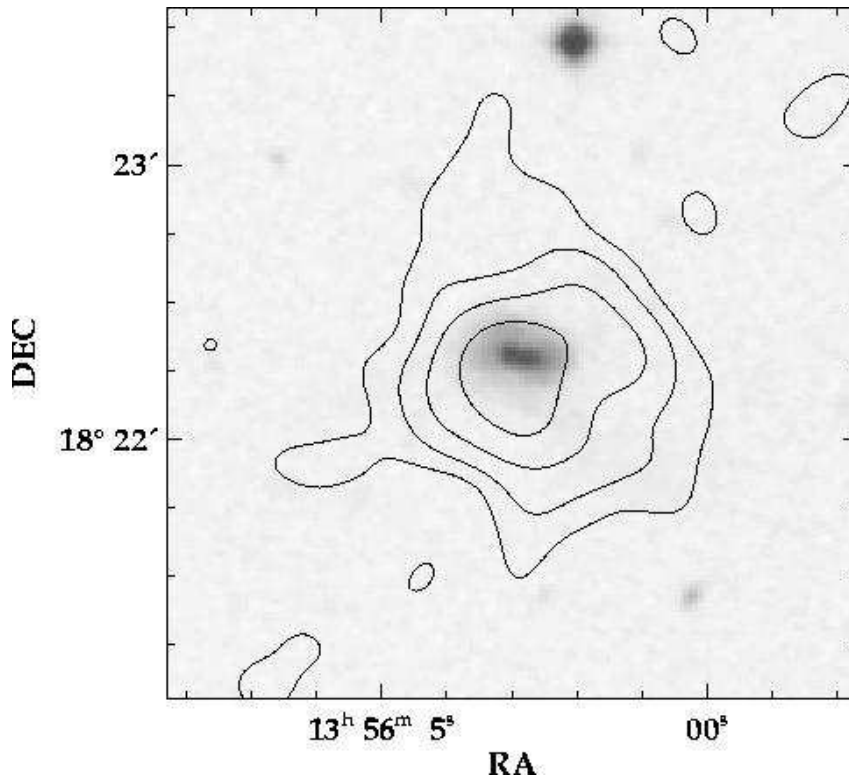


FIG. 2.— Contours of PSPC intensity overlaid on DSS image of Mrk 463. The X-ray data have been smoothed by $\text{FWHM}=15''$. The contour intervals are logarithmically spaced by factors of 2, beginning with 3σ above the background.

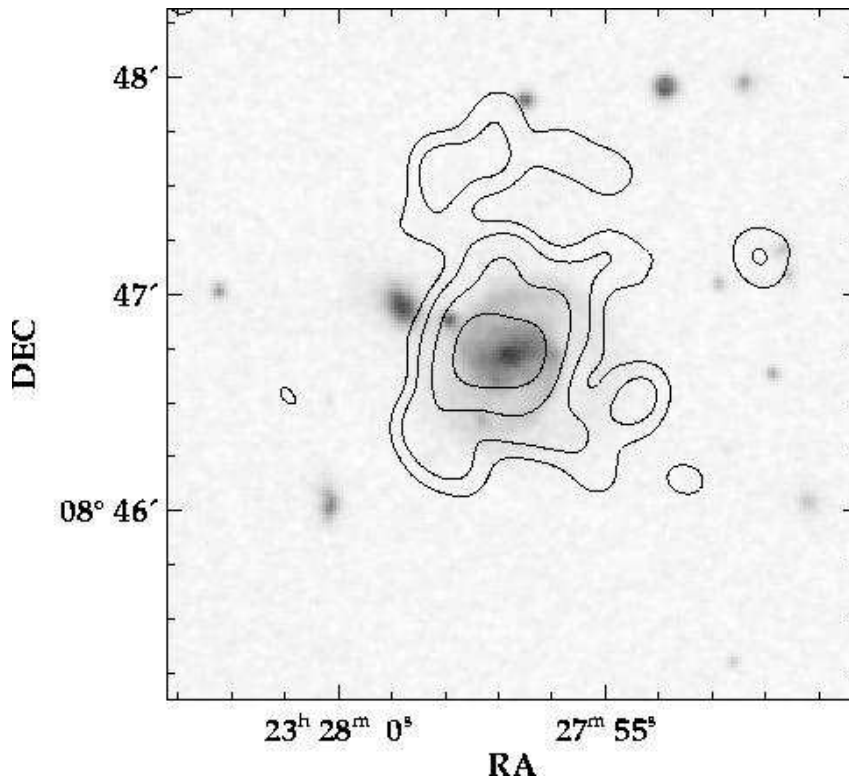


FIG. 3.— PSPC contours overlaid on DSS image of NGC 7674. The X-ray data have been smoothed by $\text{FWHM}=15''$. The lowest contour level is 3σ above the background, and the interval is spaced logarithmically by factors of 2.

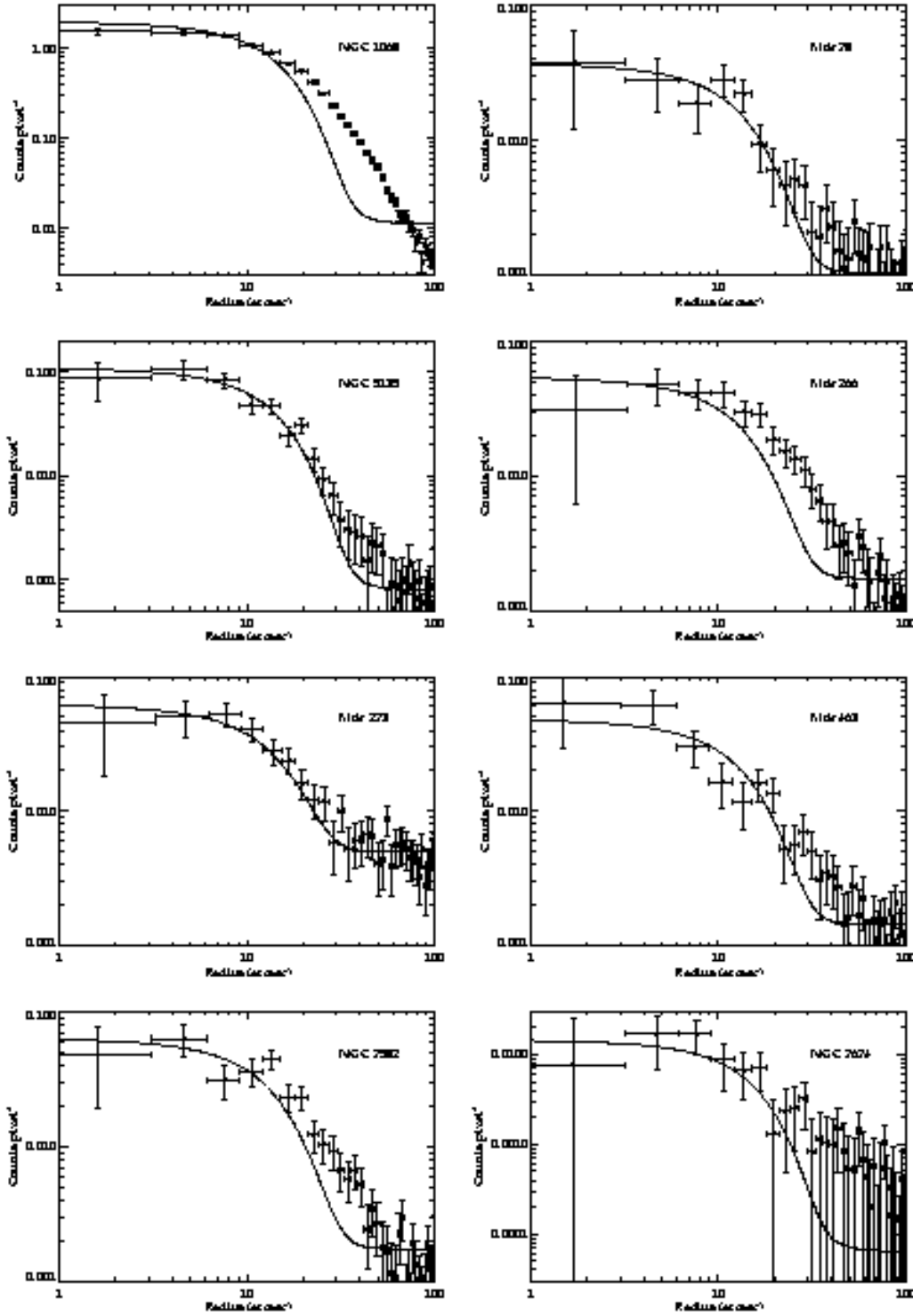


FIG. 4.— Radial profile of X-ray emission detected with *ROSAT* PSPC. Data points are azimuthal averages of counts per raw ($0''.5$) pixel. The background and amplitude are fit to the theoretical point-spread function (*solid line*). As labelled, panels show NGC 1068, Mrk 78, NGC 5135, Mrk 266, Mrk 273, Mrk 463, NGC 7582, and NGC 7674 sequentially.

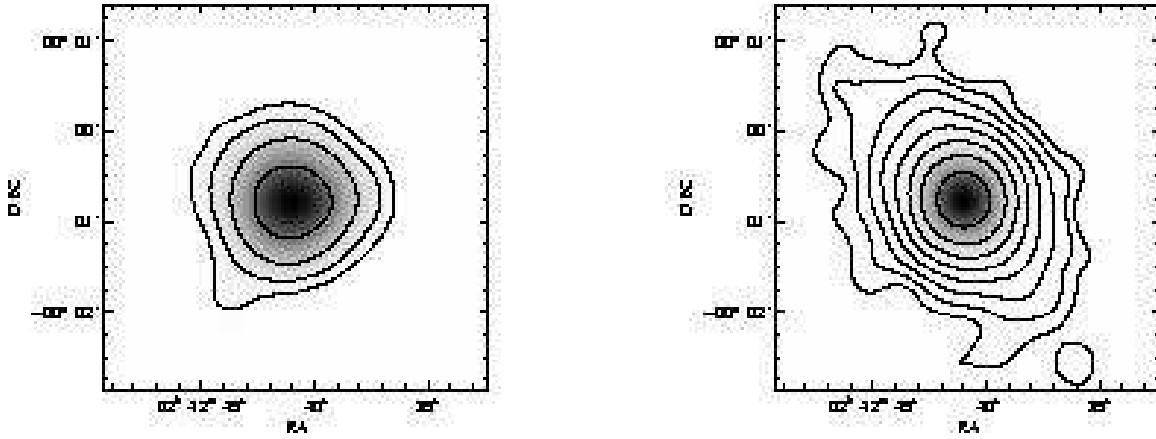


FIG. 5.— (a) Soft PSPC (0.1–0.4 keV) observation of NGC 1068, smoothed by a Gaussian of FWHM=25". The image is scaled linearly from a minimum of 1σ above the background. The lowest contour level is 2σ above the background, and the interval is spaced logarithmically by factors of 2.5. (b) Hard PSPC (0.4–2.1 keV) observation of NGC 1068, with the same image and contour scaling described in (a). The spatial distributions of the two energy bands are distinct. The harder emission is more centrally concentrated, and the elongation directions are nearly perpendicular to one another.

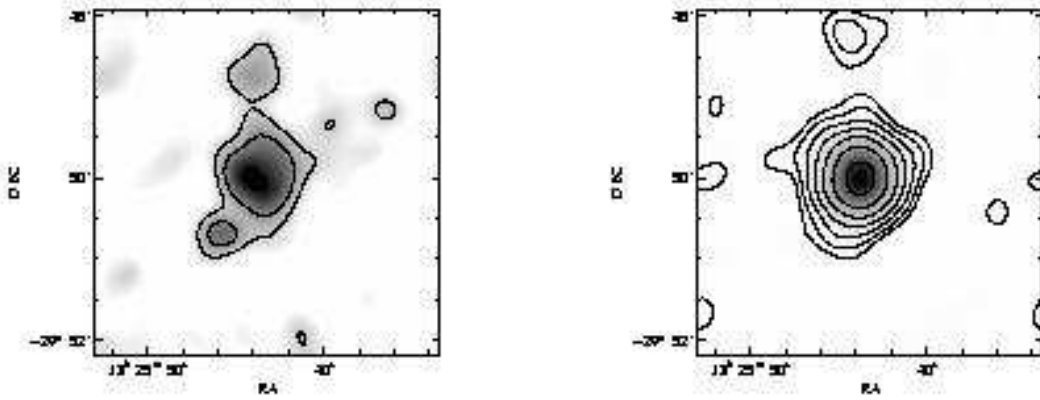


FIG. 6.— (a) Soft PSPC (0.1–0.4 keV) image of NGC 5135, smoothed by a Gaussian of FWHM=25" and scaled linearly from a minimum of 1σ above the background. The lowest contour level is 4σ above the background, and the interval is spaced logarithmically by factors of 2. (b) Hard PSPC (0.4–2.1 keV) image of NGC 5135, with smoothing, scaling and contour levels as described in (a).

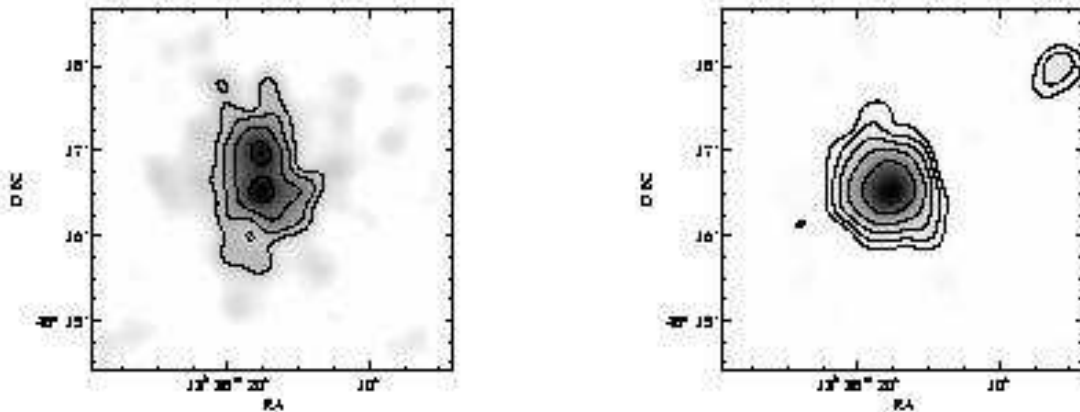


FIG. 7.— (a) Soft PSPC (0.1–0.4 keV) image of Mrk 266, smoothed by a Gaussian of FWHM=20". The image is scaled linearly from a minimum of 1σ above the background. The lowest contour level is 5σ above the background, and the interval is spaced logarithmically by factors of 2. (b) Hard PSPC (0.4–2.1 keV) observation of Mrk 266, with the same image and contour scaling described in (a). The nuclei of Mrk 266 are the principal components of the harder emission, while both the nuclei and the extended emission north of them are significant at softer energies.

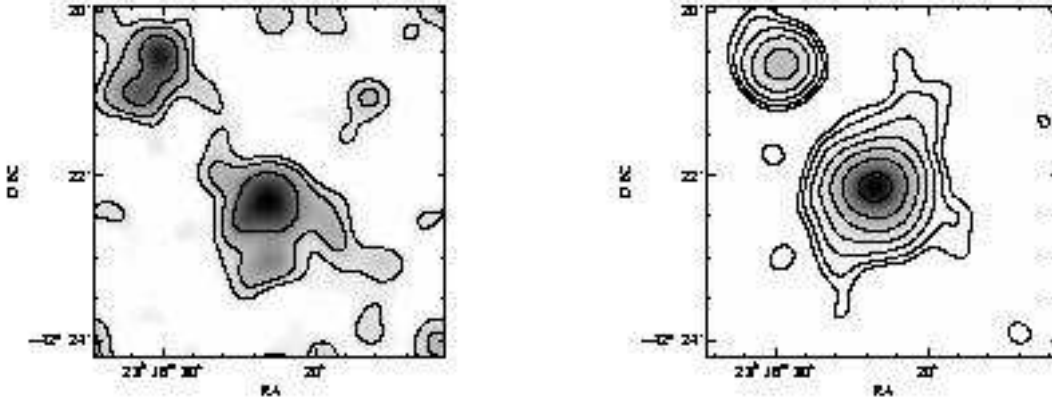


FIG. 8.— (a) Soft PSPC (0.1–0.4 keV) image of NGC 7582, smoothed by a Gaussian of FWHM=25". The image is scaled linearly from a minimum of 1σ above the background. The lowest contour level is 3σ above the background, and the interval is spaced logarithmically by factors of 2. (b) Hard PSPC (0.4–2.1 keV) observation of NGC 7582, with the same image and contour scaling described in (a). The softest emission is extended preferentially perpendicular to the galactic disk. The harder emission is more centrally concentrated and more extended in the plane of the galaxy.

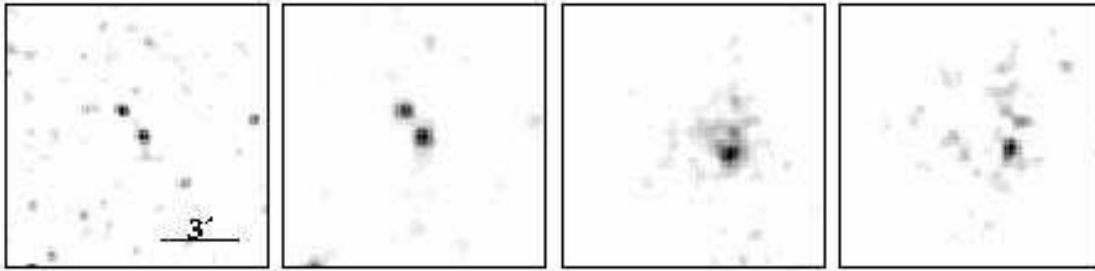


FIG. 9.— Mrk 273 in *ROSAT* HRI, *ROSAT* PSPC (0.5–2 keV), *ASCA* SIS0 soft (0.5–2.0 keV), and *ASCA* SIS0 hard (2.0–10 keV) bands. These approximately aligned images illustrate that the companion galaxy, located about 2' northeast of Mrk 273, faded from the time of the PSPC observation (1992 June) to the time of the *ASCA* observation (1994 May). Although the extracted *ASCA* spectra include the companion, it does not contribute significantly to the measured flux.

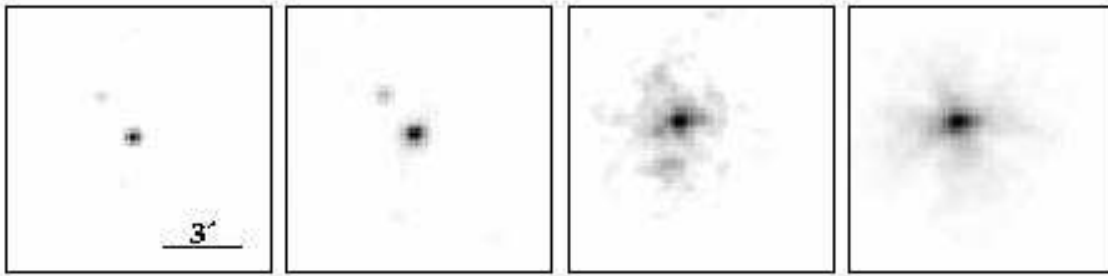
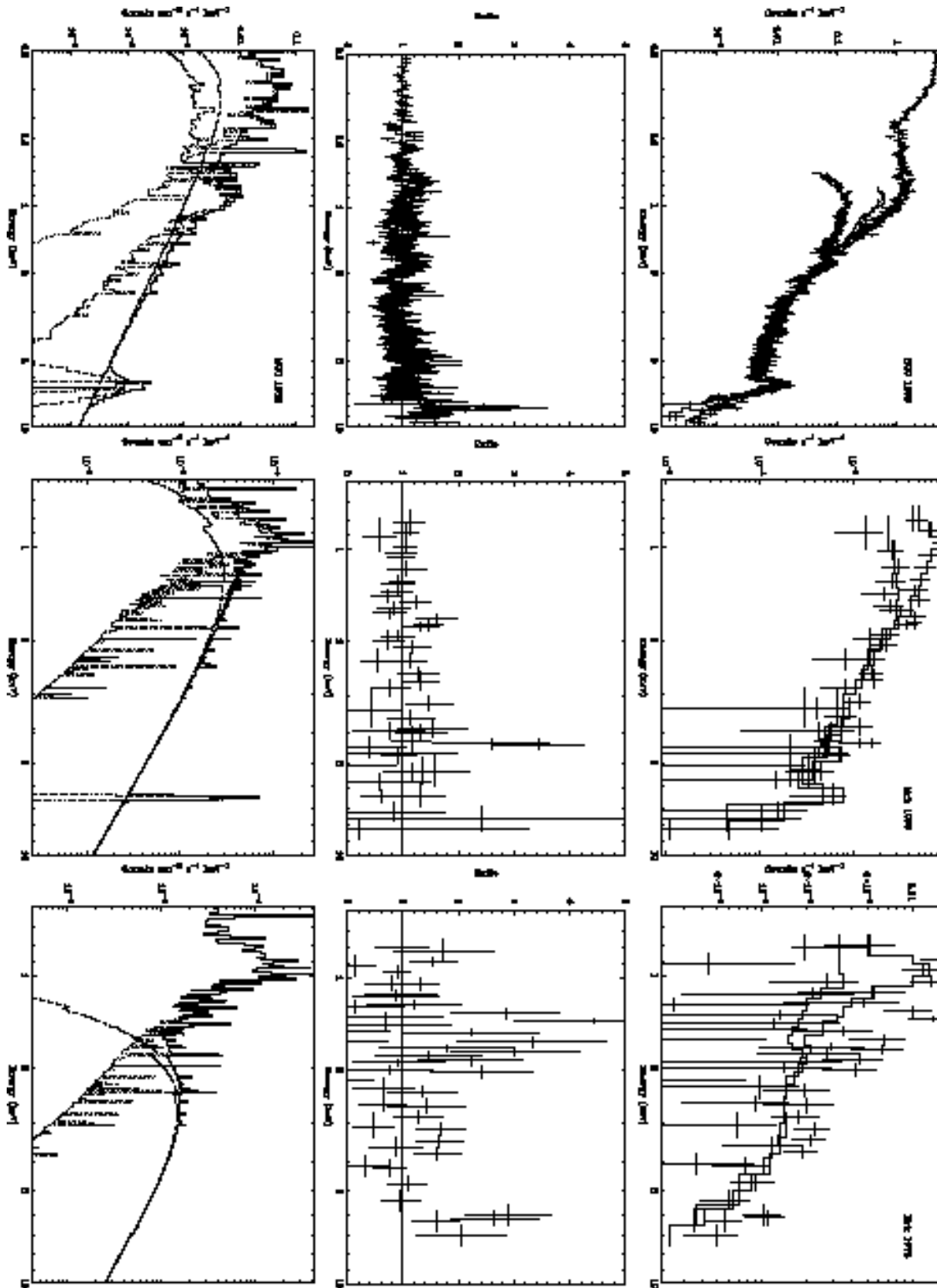
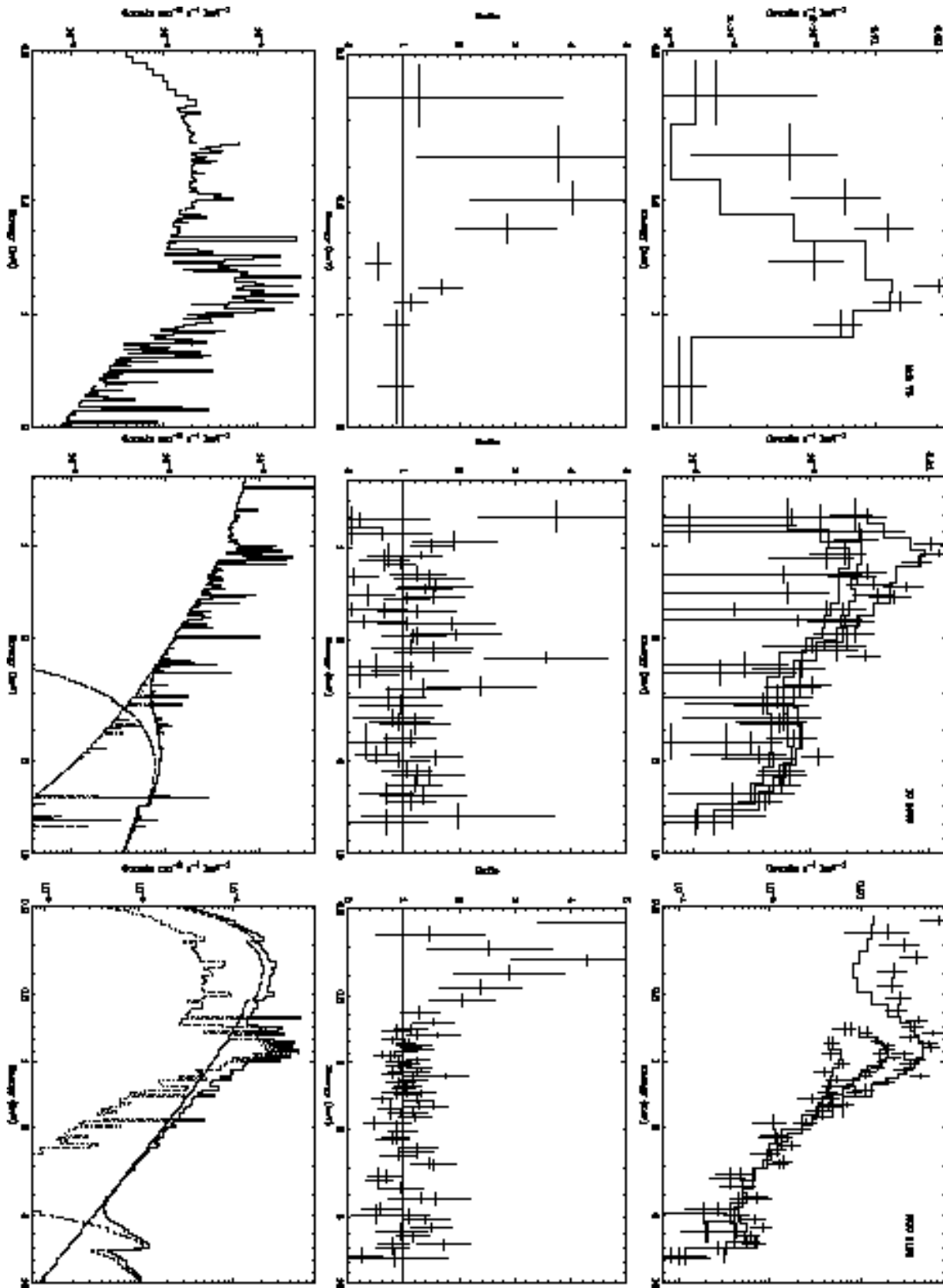
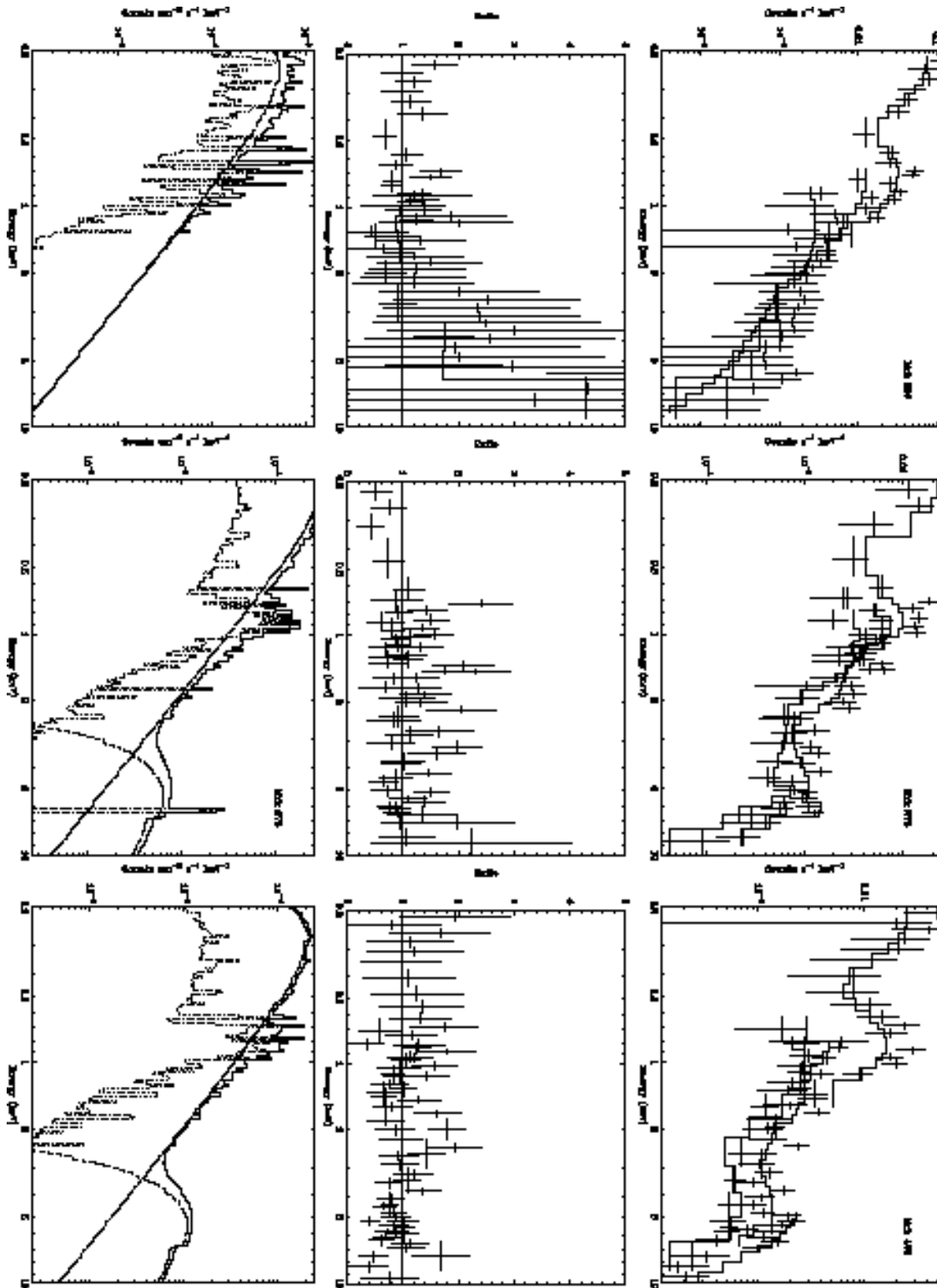
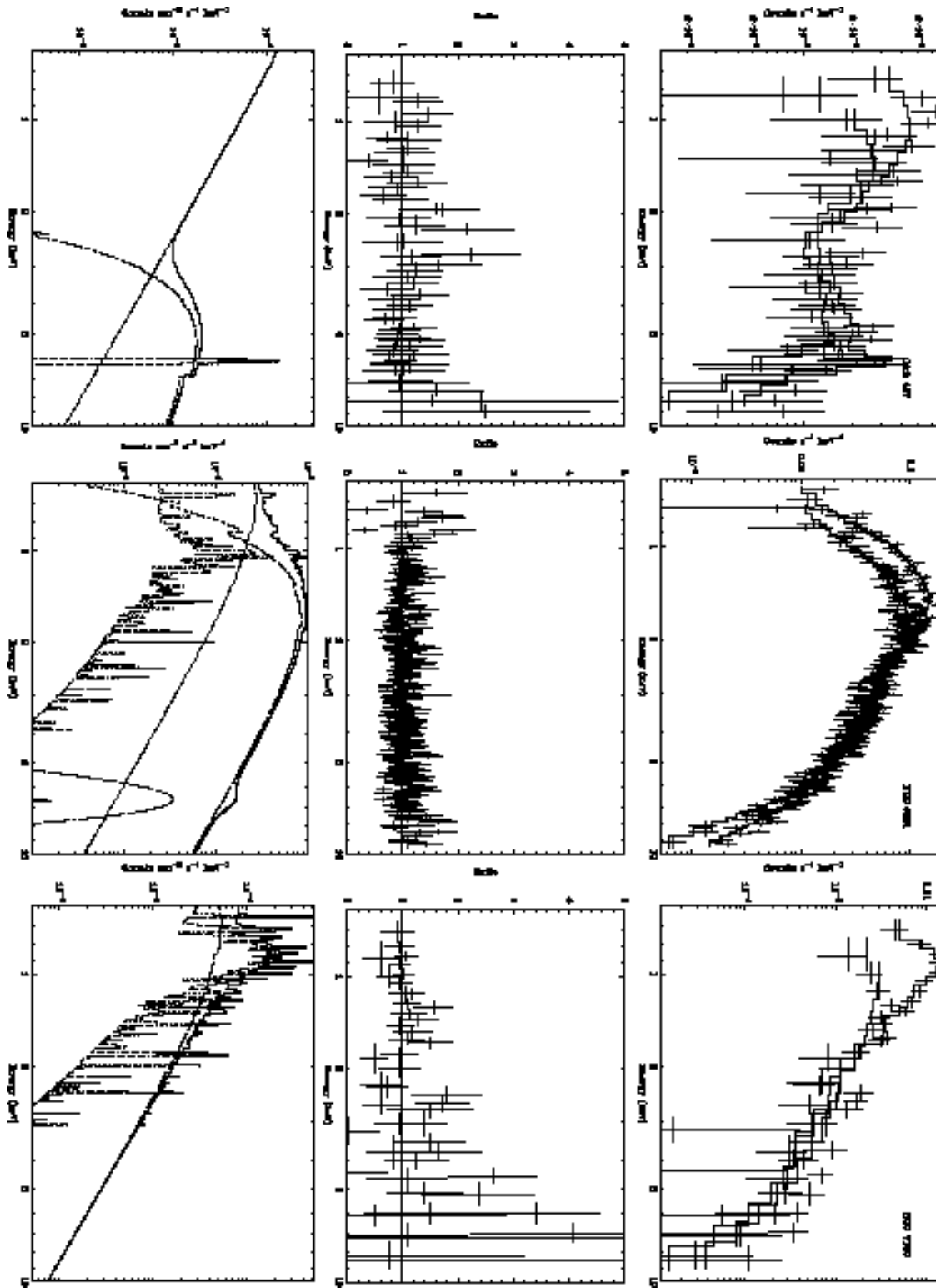


FIG. 10.— NGC 7582 in *ROSAT* HRI, *ROSAT* PSPC, *ASCA* SIS0 soft, and *ASCA* SIS0 hard bands. The soft spectrum of the companion of NGC 7582, located about 2' toward the northeast, does not significantly contaminate the *ASCA* spectra in the observation from 1994 or 1996 (shown).









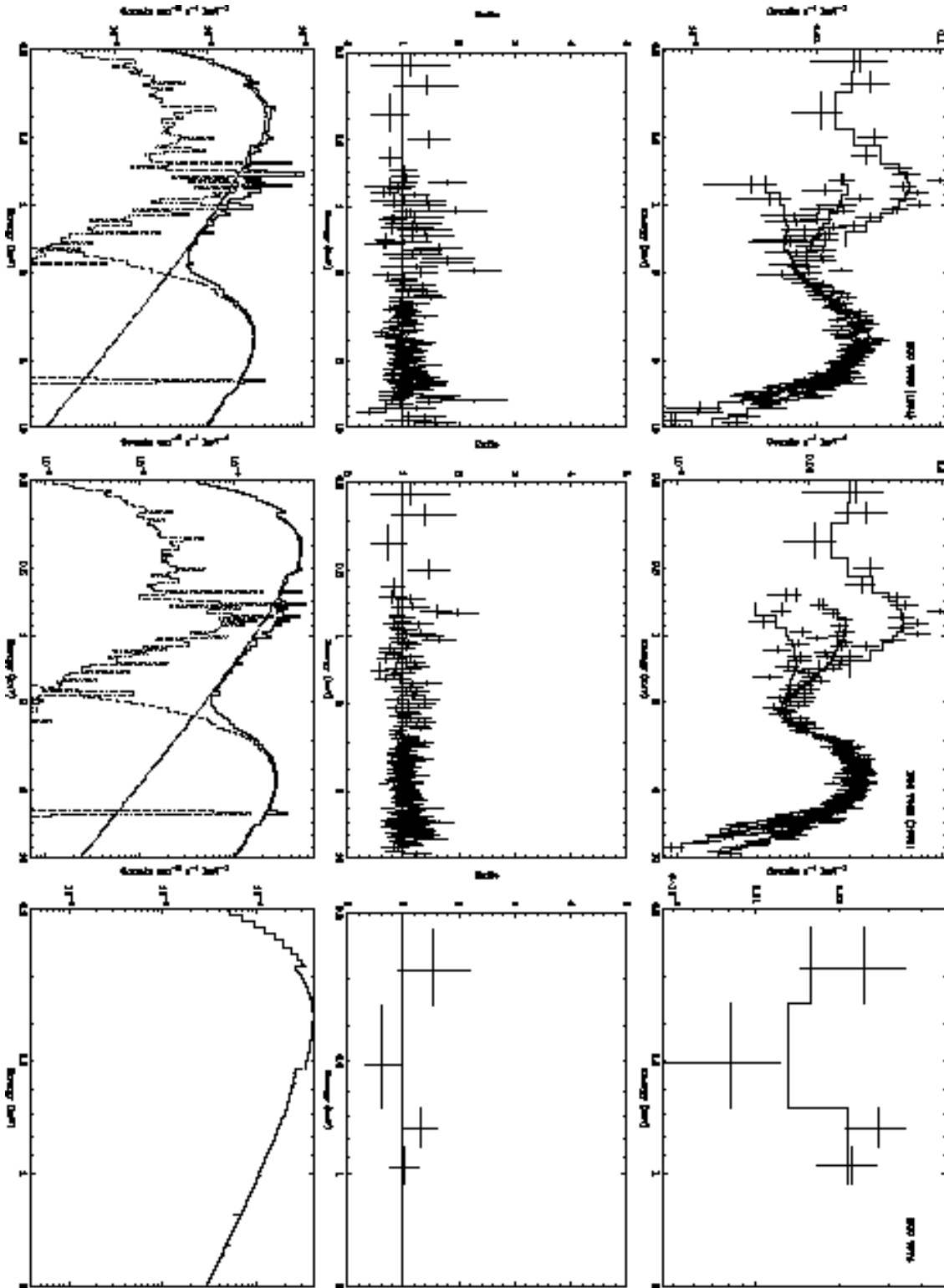


FIG. 11.— X-ray spectra of Sy2/SB composite galaxies. For each galaxy, the top panel contains the data and best-fitting model folded through the instrument response. The SIS0 and SIS1 data are combined for plotting purposes, as are the GIS2 and GIS3 data. PSPC data are also included in the relevant instances. The second panel contains the the ratio of the data to the model. The bottom panel contains the total model spectrum at higher resolution (*solid line*) and the individual model components (*broken lines*).

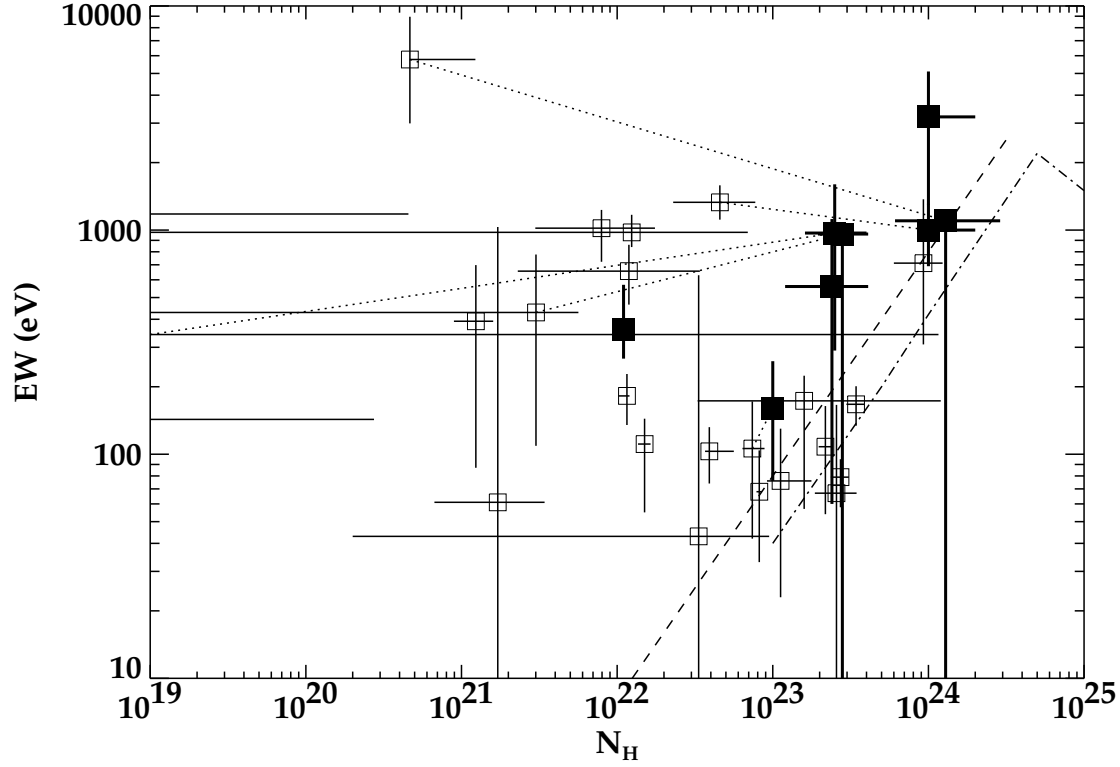


FIG. 12.— Fe K equivalent width vs. N_H for our sample (*solid symbols*). For comparison, we also plot the results from Turner et al. (1997; *open symbols*), which were derived using the observed continuum. Common objects in the two samples are connected with dotted lines. Theoretical predictions for spherically-symmetric (*dashed line*; Awaki et al. 1991) and torus (*dot-dashed line*; Ghisellini, Haardt, & Matt 1994) geometries are also plotted. Although we cannot distinguish between these two models, our results are generally consistent with both of them.